KTH Engineering Sciences

Investigation of the WW excess observed by ATLAS and CMS at the LHC

Katarina Atteryd

atteryd@kth.se

Master of Science Thesis

Supervisor: Jonas Strandberg
Examiner: Bengt Lund-Jensen

TRITA-FYS 2015:62
ISSN 0280-316X
ISRN KTH/FYS/–15:62-SE

Stockholm, Sweden

September 12, 2015

Abstract

In the $H \rightarrow WW \rightarrow l\nu l\nu$ decay mode of the Higgs analysis, there is a discrepancy between the observed and predicted SM WW background cross sections. The observed WW cross sections at CMS and ATLAS are measured to be 20 % higher than the SM prediction and are more consistent with each others measurements than with the theoretical predictions. No similar excess or discrepancy has been seen for other backgrounds in the Higgs analysis, suggesting there is no simple answer to this problem. Possible explanations, that appeared in the literature during the year of 2014, are deficiencies of the theoretical calculations of the SM WW cross section. Investigations was also carried out by the author looking for irregularities in the kinematic shapes in the Higgs analysis, in order to systematically classify the excess. No tendencies of shape variations was found except for in the m_{ll} distribution.

The theoretical developments during the last year manages to explain part of the excess but not all of it. There is still no explanation to the shape discrepancy in the m_{ll} distribution.

Sammanfattning

I Higgsanalysens $H \rightarrow WW \rightarrow l\nu l\nu$ sönderfallskanal verkar det finnas en skillnad mellan de observerade och teoretiskt framräknade tvärsnitten för SM WW bakgrunden. De observerade tvärsnitten från CMS och ATLAS mättes till 20 % högre än standardmodellens förutsagda värde och verkar vara mer i linje med varandras värde än de teoretiskt beräknade. Inget liknande överskott eller avvikelse går att se i andra bakgrunder för Higgsanalysen, vilket innebär att det förmodligen inte finns ett ensamt enkelt svar på problemet. Tänkbara förklaringar, framlagda under 2014, är brister i de teoretiska beräkningarna av SM WW tvärsnittet. Undersökning genomfördes även genom att titta efter avvikelser av de kinematiska distributionerna i Higgsanalysen, i syfte att systematiskt kunna klassificera överskottet. Inga tendenser till avvikelser kunde konstateras förutom i m_{ll} distributionen. Studierna av överskottet som genomförts under året kunde förklara en del av överskottet men inte hela. Det finns fortfarande heller ingen förklaring till avvikelsen i m_{ll} distributionen.

Contents

Chapter 1

Introduction

On July 4 in 2012 CERN announced the discovery of the Higgs boson [1][2]. This marked the end of a 50 year long era in trying to find the last piece missing of the Standard Model in particle physics.

There seemed to be a problem however in the cross section measurement of the SM WW background in the analysis of the Higgs boson decaying into a pair of W bosons. In both CMS and ATLAS, the measured WW cross section was found to be 20% higher than the Standard Model prediction. In the ATLAS Higgs to WW analysis, the predicted cross section was multiplied by a factor of 1.2 and the problem was ignored until the summer of 2014 [3][4].

The aim of this thesis is to investigate this excess discrepancy and try to do a systematic classification of the problem. This is done by analysing the kinematic distributions with dominating WW background in the $H \to WW$ analysis.

This discrepancy suddenly became a popular subject of interest in the summer of 2014 and three independent studies that are trying to explain the excess by finding deficiency in the theoretical calculations of the cross section has been followed and analysed in this thesis.

1.1 Outline

This thesis will begin with an introduction of the Standard Model of particle physics and the Higgs mechanism in chapter 2 and continue with a brief presentation of the LHC and the ATLAS detector with its components in chapter 3. The Higgs phenomenology of production and decay channels will be described in chapter 4 and then followed by a discussion of the Higgs analysis strategy in chapter 5. The main focus of this thesis is in chapter 6 where the excess discrepancy is summarised and explained. This chapter also contain possible explanations from other studies of the problem and discussion about shape variations of different kinematic distributions from the Higgs analysis. Finally, conclusions of the thesis is presented in chapter 7.

1.2 Author's contribution

This thesis has been a literature study in investigating the excess of WW bosons observed by ATLAS and CMS at the LHC in both analyses of the Higgs boson decaying to WW and in measurements of the WW cross section. ATLAS and CMS papers describing these measurements [5][6][7][8] have been studied, and distributions have been compared and searched for any systematic shift between measurement and prediction which could help explain the overall discrepancy. This was the starting point for further investigations, and it is documented in Chapter 6.

The WW background in the ATLAS Higgs analysis has been studied in more detail. Time was spent understanding the analysis, including the list of event selection and the philosophy behind the choices made in the analysis. After understanding the various stages of the selection, kinematic distributions of the WW background at all levels of the cut flow were studied and comparisons were made between the measured distributions and the predictions.

Special attention was paid to differences that could not be explained by a simple scaling of the WW cross section, and one important such distribution was identified where there is a clear shape difference between the data and the predicted shape. Only a tiny sample of all the distributions looked at are reported in this thesis, selected to exemplify the overall trends noticed when studying the complete set of plots.

In the beginning of this thesis work, the problem of observed excess became a hot topic for others as well. A major part of this study has therefore been to follow the progress of others, read about possible explanations put forward in various papers, and finally sort out the most plausible explanations. The most important theoretical papers concerning the WW excess published during my master thesis studies are summarised in Chapter 6.

Chapter 2

The Standard Model

The Standard Model of particle physics is a theory comprising all fundamental constituents of matter and their interactions.

The history of the Standard Model began in the late 19^{th} century when it became clear that atoms in fact are not indivisible. One major step towards a new paradigm was the discovery of the electron in 1897, the first elementary particle to be discovered. A positive nucleus would not be verified until 1909 and it would take ten more years before the discovery of the proton [9].

The quark model was formulated by Murray Gell-Mann in 1964 where the first discovered hadrons all consisted of three quarks: up, down and strange. The idea of combining the forces into one unique theory has long been pursued throughout the century and a first step closer to this came when Sheldon Glashow unified the electromagnetic and the weak force [10]. In 1967, Abdus Salam and Steven Weinberg incorporated the Higgs mechanism with Glashow's electroweak theory and for this the three of them received the Nobel prize in 1979 [11].

The Higgs mechanism explained the broken symmetry of massless photons and heavy weak bosons in the Standard Model. It was put forward in independent papers by Francois Englert, Robert Brout and Peter Higgs in 1964 [12][13]. In November the same year a paper explaining the Higgs mechanism further was presented by Carl R Hagen, Gerald Guralnik and Tom Kibble [14]. Since the last three referred to the papers written earlier that year it was Englert and Higgs that received the Nobel Prize in 2013 after the discovery of the Higgs boson at CERN in 2012.

The Standard Model began to be well accepted when Gerard 'tHooft proved how the theory could be renormalisable [15], which he received a Nobel Prize for in 1999 shared with his advisor Martinus Veltman.

Although the Standard Model have generated a couple of Nobel Prizes and have been experimentally verified to great precision, the theory is still not a complete theory of nature. The gravitational force is for example not included in the theory. Measurements of rotational curves of galaxies show existence of dark matter for which the particles of the Standard Model cannot explain. Finally, neutrino oscillations is a proof of neutrinos having mass, which is not the case in the Standard Model [16]. However, it is still a very successful theory despite its deficits.

2.1 Particles

The Standard Model is a theory in which all elementary particles and forces, except gravity, are included. There are three distinct sectors of the model divided by the spin of the particles. Fermions with half-integer spin, gauge bosons, which are called "force carriers", with integer spin, and the Higgs Boson, which today is the only detected particle with zero spin [17].

Fermions follow Fermi-Dirac statistics and are subjects to the Pauli-exclusion principle, it means that two identical fermions cannot simultaneously occupy the same quantum state. All fermions have a corresponding antiparticle with the same mass and spin but opposite charge. The fermions are divided into three generations, see figure 2.1, where the first generation contains the lightest, and therefore the stable particles. Hence all stable matter in the universe are combinations of particles from the first generation, this is due to the fact that particles decay from higher to lower generations. Furthermore the fermions are divided into leptons, fermions that do not partake in strong interactions, and quarks, fermions that do.

Bosons on the other hand follow Bose-Einsteins statistics and may be either elementary or composites of quarks. The Standard Model contains five elementary bosons, the four gauge bosons with spin-one; photons, gluons, W and Z bosons, and the Higgs boson with spin-zero. Gauge bosons mediate interactions between all particles, whereas the Higgs bosons is responsible for giving particles their mass [9].

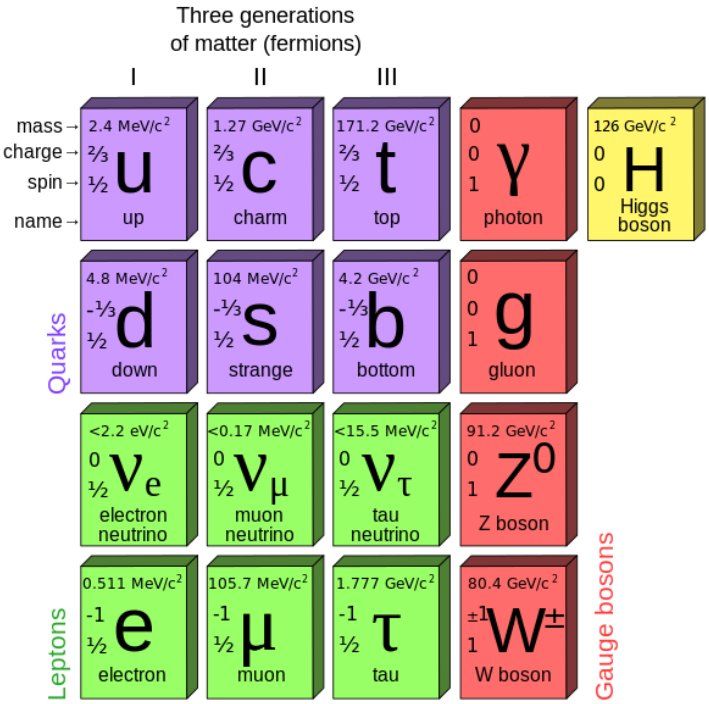

Figure 2.1: The Standard Model of particle physics divided in fermions and bosons. Fermions are categorised in quarks and leptons, both sorted in three generations. Bosons consists of the four gauge bosons and the Higgs boson.

2.1.1 Leptons

Leptons are fermions that do not undergo strong interactions. Each generation of leptons have a lepton number and contains a charged lepton and a neutrino. The leptonic number must be conserved in all interactions and is set to 1 per flavour but have the opposite sign for the corresponding antiparticle.

The charged leptons have both electromagnetic interactions as well as weak interactions. The most well known charged lepton is the electron in the first generation. The heavier leptons in the second and third generation are the muon, μ and tau, τ.

Neutrinos on the other hand have no charge and are treated as massless particles in the Standard Model. This has been proven to be false though since there are strong evidence of neutrino oscillations. Because of their neutral charge, they only interact weakly and can easily pass through the earth. They are thus hard to detect and are instead detected through an imbalance in energy and momentum in detectors [18].

2.1.2 Quarks

The other group of fermions are quarks. In comparison to leptons they can, besides interacting with the electromagnetic and the weak force, also undergo strong interaction.

The Standard Model contains 6 quarks; up, down, charm, strange, top and bottom, these are divided in the same three generations as leptons. Every generation consists of two quarks with charges $+\frac{2}{3}$ and $-\frac{1}{3}$.

Quarks cannot be detected freely, they only exist in compositions called hadrons. There are two bound states of hadrons in which quarks occur; mesons that are built up by quark and antiquark ($q\bar{q}$), and baryons that are built up by three quarks (qqq) or ($\bar{q}\bar{q}\bar{q}$).

Similar to the lepton number each quark have a baryon number of $\frac{1}{3}$ and the baryon number must be conserved in all interactions. The antiquark have opposite sign both for the charge and the baryon number.

Protons and neutrons are the two most common examples of baryons and are compositions of the two quarks from the first generation, the up and the down quark, see figure 2.2 [18].

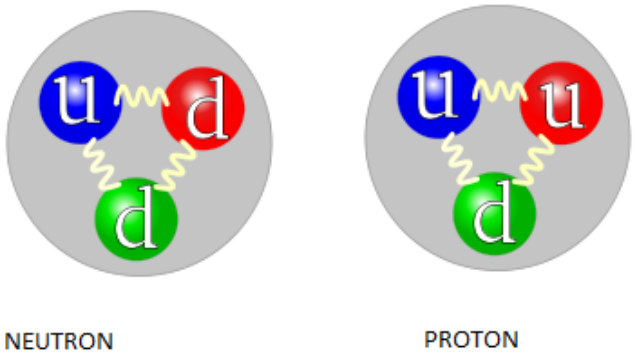

Figure 2.2: Quark composition of a neutron and a proton held together with gluons. The neutron consists of one up quark and two down quarks, whereas the proton consists of two up quarks and one down quark.

2.2 Interactions

There are four known fundamental forces in the universe; the electromagnetic force, the weak force, the strong force and gravity. The first three of these forces are included in the Standard Model. Gravity is insignificant on quantum level and does not contribute any noticeable effects in particle physics and is therefore not included.

The three forces in the Standard Model are responsible for all interactions between particles and are carried by their "force carriers", as can be seen in figure 2.3. These mediating particles are known in the Standard Model as gauge bosons and have the range of inverse proportional to its mass [19].

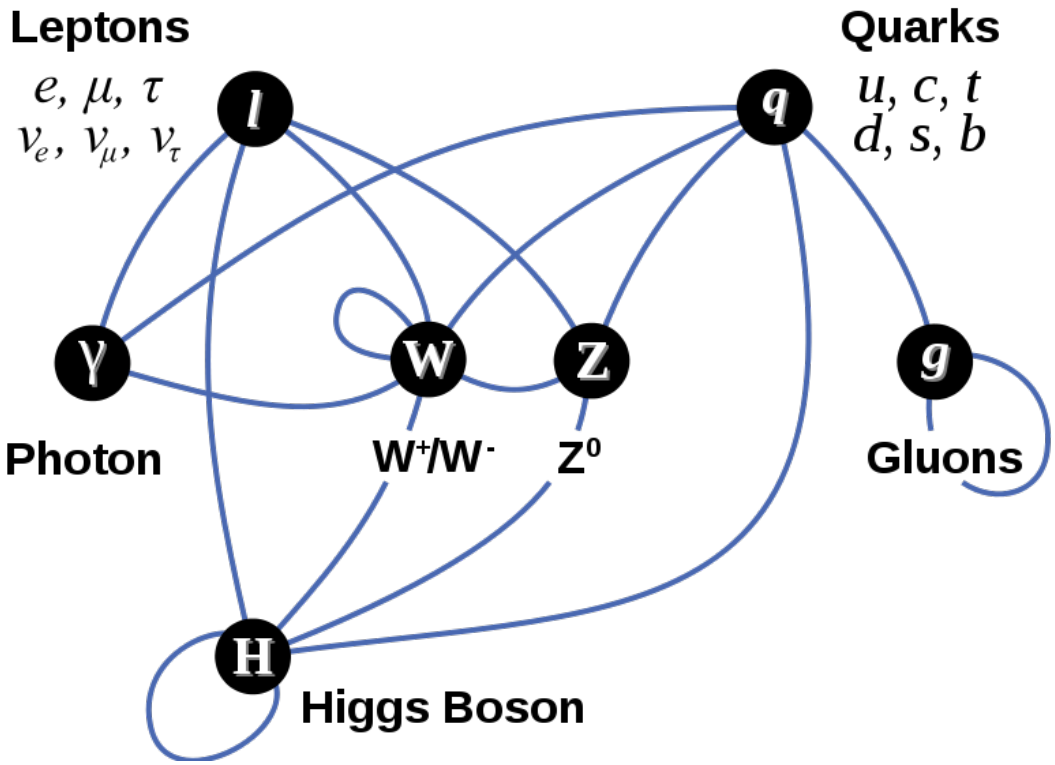

Figure 2.3: Interactions between particles described by the Standard Model. The Higgs boson, responsible for giving particles its mass, interacts with all particles except for the massless gluons and photons. Leptons interacts weakly and with the electromagnetic force, whereas quarks can partake in all interactions.

2.2.1 Electromagnetism

The most famous force included in the Standard Model is the electromagnetic force and is in general known for being the interaction responsible of keeping electrons bound to the positive charged nucleus in atoms.

The electromagnetic force is mediated by photons and couples to all electrically charged particles, such as charged leptons, quarks and $W^{\pm}$ bosons. The photon has no electric charge and therefore does not couple to itself, as can be seen in figure 2.3. Furhtermore, they are massless particles and because of this have infinite range.

2.2.2 Strong Interaction

The strong force is mediated through eight kinds of gluons. Similarly to the photon, the gluons have no mass or electric charge. In addition to this, the gluons carry a colour charge They therefore couple with the colour charged particles in the Standard Model which are quarks and themselves, as seen in figure 2.3. The strong force is thus the only force that couples exclusively to only one of the two categories of fermions in the Standard Model.

Colour is a charge that is carried by quarks and gluons and is conserved in all strong interactions. There are three existing colours; red, green and blue, and corresponding anti-colours. However, hadrons are always colourless which is why no free quarks exists, and the reason for creating jets, composite quarks, in detectors. This is called confinement.

Strong interaction is responsible for binding quarks together into hadrons. It is stronger at lower energies and weaker when decreasing the distance. This unusual property of a force is called asymptotic freedom.

2.2.3 Weak Interaction

The weak force is the only force that can change flavours in the Standard Model. It is mediated by three heavy gauge bosons; the neutral Z^0- boson and the two charged $W^{\pm}$-bosons. Since the bosons mediating the force are massive, it is very short ranged.

Flavour changing interactions are mediated by the $W^{\pm}$-bosons. These interactions are called charged current interactions since particles have to change their charge when decaying and mediating with one of the two charged W-bosons [20].

The W-boson only couples to left-handed particles, which for a particle travelling at the speed of light means that ts momentum is in opposite direction to its spin. The Z^0-boson on the other hand can couple to both right- and left-handed particles. It also conserves flavour in interactions which are called neutral current interactions.

The weak force is thus the force responsible for elementary particles decaying , like in the radioactive beta-decay for example. It can interact with leptons, quarks and themselves and is therefore the only force in the Standard Model that can interact with all matter particles.

2.3 The Higgs mechanism

The Standard Model is a renormalizable quantum field theory and eliminates infinite contributions by reparameterizing for example electric charge and mass in order to get finite solutions. This has created problems throughout the last century when trying to find a solution to why particles have mass.

According to Chen Ning Yang and Robert Mills in 1954 all fundamental forces were merely results of nature maintaining its symmetries. Yang and Mills tried to apply quantum field theory to strong interactions by proposing three new particles, B^+, B^- and B^0. These had to be massless for the theory to be renormalisable [15].

Julian Schwinger suggested the same solution but applied it to weak interactions instead. His graduate student Sheldon Glashow continued with the theory and managed to unify the electromagnetic theory with the weak theory, at high energy scales, into what

is now known as the electroweak theory. Similar to Yang and Mills, Glashow proposed three massless weak vector bosons carrying the force. Two of them with electric charge, W^+ and W^-, and the third a neutral particle to account for interactions where no charge is transfered. The electroweak unification also predicted weak neutral current mediated by the proposed Z^0-particle. This would not be experimentally confirmed until 1973.

At the same time Yoichiro Nambu attended a seminar in which superconductivity was discussed. Application of quantum theory was used to describe why particles did not retain fixed positions and why electrons still had motion in the lowest energy state, i.e. the vacuum state, as was expected. The theory did not seem to conserve the electric charge and therefore not respect the gauge invariance of the electromagnetic field.

Yoichiro Nambu realised that this was an example of spontaneous symmetry breaking where the additional energy appeared as mass. This promised a solution for the initial problems of massless gauge bosons in the Standard Model.

Symmetry breaking can be described as phase transitioning where the field is non-zero at the minimum. An example of a broken symmetry is having a marble balancing on top of a sombrero, as seen in figure 2.4. It is perfectly symmetrical but unstable. The marble will randomly roll down a specific direction and come at rest, the symmetry is now said to be ”broken”. A better word to explain it is that the symmetry is "hidden" from the marble but is of course still there.

It would not take long until a series of papers explaining the mechanism of spontaneous symmetry breaking leaving massive particles. Independently of each other in the year 1964, Robert Brout and Francois Englert, Peter Higgs, and Gerald Guralnik, Carl Hagen and Tom Kibble, published three papers describing what later came to be called the Higgs mechanism, or BEH-mechanism for Brout-Englert-Higgs [21].

The BEH-mechanism managed to maintain gauge invariance when creating massive gauge bosons while still being renormalisable. The first paper by Peter Higgs was actually rejected. When revising the article he added a sentence in the end of the paper implying the existens of one (or more) new massive scalar bosons. This would be the Higgs boson that was discovered at CERN in the summer of 2012 [22].

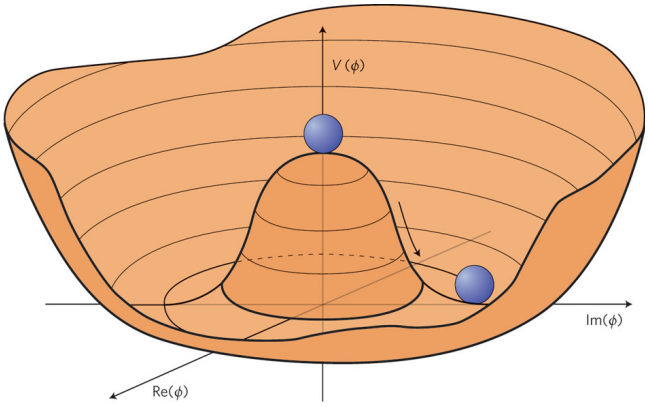

Figure 2.4: The potential of the Higgs field also known as ”the mexican hat potential”. It has an infinite number of ground states since the origo is not a minima and is responsible for the mass of the weak bosons and heavy fermions in the Standard Model. Figure credit [23].

2.4 Feynman diagrams

When calculating the probability of interactions between particles the transition amplitude is needed [24]. This requires large and complicated integrals. Richard Feynman introduced a more graphical way to calculate the different terms in the integrals instead which came to be called "Feynman diagrams" and is now one of the most important tools used in particle physics.

Feynman diagrams represent a possible way for the interacting particles to reach the final state of the process. The basic structure can be seen in figure 2.5 and consists of lines representing particles and fields, and vertices where particles are created or annihilated. Usually time flows from left to right and the room axis is then perpendicular to the time axis. As a result of this, the initial particles of the process are to the left in the diagram and the final particles are to the right. Between these is a propagator, that is, the force mediating particle of the interaction. Fermionic particles are symbolised by an arrow pointing in the time-direction. If the arrow is pointed in the opposite direction it represents an anti-particle.

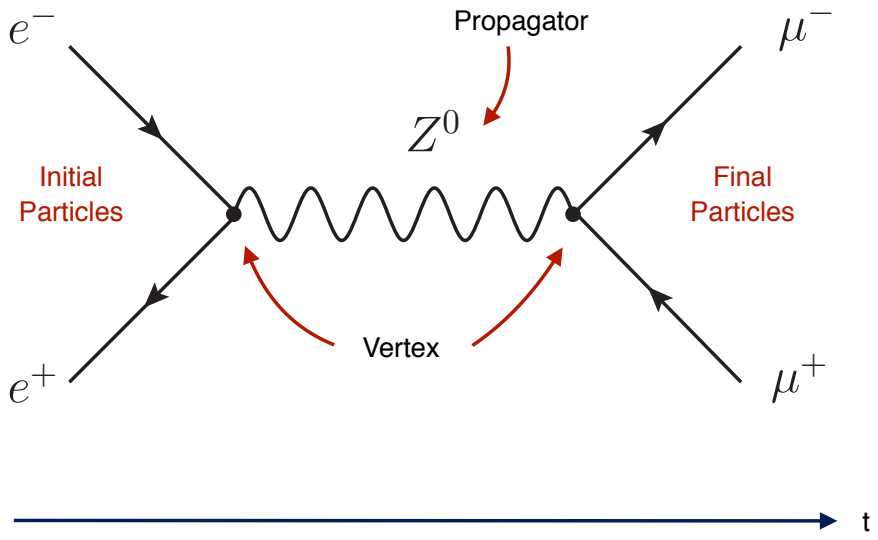

Figure 2.5: Feynman diagram showing the basic structure where e^- and e^+ are the initial particles in the process, μ^- and μ^+ are the final particles and Z^0 is the propagator mediating the weak force.

Each vertex contains a factor proportional to the square root of the coupling constant. This is a measure of the strength of an interaction between particles and the mediating force carrier. When constructing a diagram certain rules have to be followed to agree with the interactions of the Standard Model. This is true in each vertex of a Feynman diagram. However, if energy conservation is violated, the mediating particle is said to be virtual and its mass is then called off shell.

The amplitude of a diagram is calculated by multiplying the vertex factors in the diagram. A diagram of leading order represents the simplest way of interacting from the initial to the final state of particles and contains thus two vertices. The amplitude will then be proportional to the coupling constant of the interaction.

By taking the sum of contributions from different Feynman diagrams in an interaction process, a good approximation of the transition amplitude is reached without having to deal with complicated integrals. The probability of this process, also known as cross section, denoted σ, is then the transition amplitude squared.

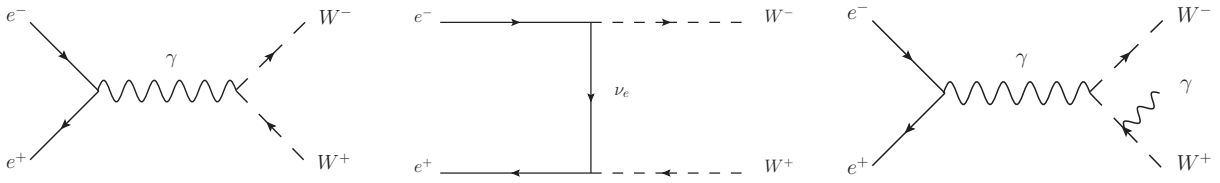

(a) $e^- + e^+ \rightarrow W^- + W^+$ *(b)* $e^- + e^+ \rightarrow W^- + W^+$ *(c)* $e^- + e^+ \rightarrow W^- + W^+ + \gamma$

Figure 2.6: The Feynman diagrams for (a) and (b) both describes the same process but with different mediators whereas diagram (c) has a different set of final particles and is therefore describing a different process.

Creating higher order of Feynman diagrams of the same process requires more vertices between the initial and final particles. These cannot be changed since that would represent another process. This is shown in figure 2.6 where the diagram (c) describes another process than (a) and (b) even though it looks similar.

Next-to-leading order, NLO, diagrams have four vertices and next-to-next-to-leading order, NNLO, have six vertices between the initial and the final particles as can be seen in figure 2.7. Depending on the order of the diagram, multiplication of the vertices creates smaller and smaller terms to the sum approximating the transitional amplitude, eventually leading to negligible contributions to the sum, even though there are many possible diagrams.

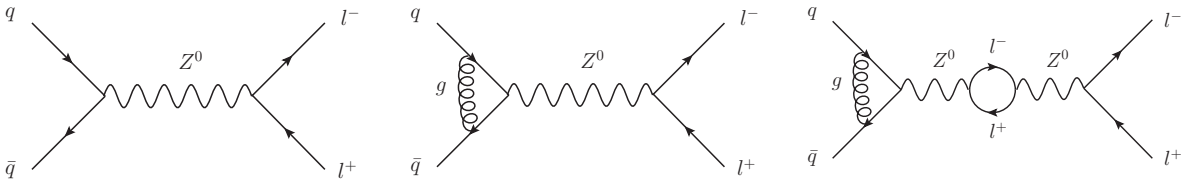

(a) LO *(b) NLO* *(c) NNLO*

Figure 2.7: Figure (a) shows a Feynman diagram of leading order, (b) and (c) describes the same process in next-to-leading order and next-to-next-to-leading order.

Chapter 3

LHC and ATLAS

CERN is today usually referred to as the European laboratory for particle physics with its home in Geneva, Switzerland, where the discovery of the Higgs boson took place in 2012.

It was established on 29 September in 1954 by 12 European founding member states in a mission to make European science world class once again, as it had been before the war. Originally CERN was an acronym for "Conseil Européen pour la Recherche Nucléaire" but changed name to "the European Organisation for Nuclear Research" when established. However, the name OERN was not as appealing as a name so they decided to keep the acronym but changed the meaning of it.

The organisation was devoted to nuclear research in the beginning, hence the name, but has currently particle physics as its main work area. The aim is essentially to enhance our understanding of the universe through fundamental research of the Standard Model and beyond. Another purpose of CERN is to bring cultures and nationalities together, and the organisation now has 21 member states with scientists from over 100 nationalities.

The research in Geneva has generated more than just new particles. It was here where the World Wide Web was first implemented and CERN has recently become a facility for grid computing [25].

CERN is today famous for being the home of the world's most powerful accelerator, the Large Hadron Collider, LHC, seen in figure 3.1. It is, with its circumference of 27 km, currently the largest scientific instrument in the world [26].

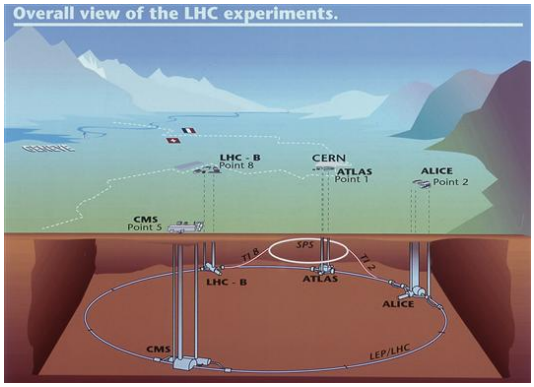

Figure 3.1: View of the LHC experiments built on the border of Switzerland and France and the locations of the four detector experiments; ATLAS, CMS, ALICE, and LHCb. (Image courtesy of CERN)

3.1 LHC

The Large Hadron Collider, more famously known as the LHC, is located on the border of Switzerland and France in Geneva and was built by CERN between 1998 and 2008 in the former LEP-tunnel (Large Electron Positron collider). It has a circumference of 27 km and is positioned between 45 to 170 m under ground in order to be shielded from cosmic rays.

The protons accelerated in LHC are retrieved by stripping electrons from hydrogen atoms. Before being injected into LHC the protons are prepared by a series of accelerators, as can be seen in figure 3.2, increasing their energy starting in Linac2. From Linac2 the protons are sent to the Proton Synchrotron Booster (PSB) where the beam of protons is accelerated up to 1.4 GeV. After PSB they will further increase their energy in the Proton Synchrotron (PS) up to 25 GeV and the finally injected into the Super Proton Synchrotron (SPS).

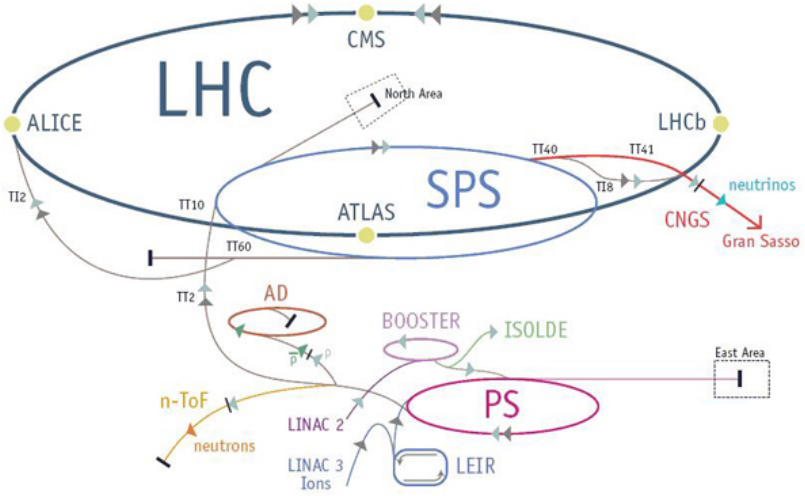

Figure 3.2: View of the accelerating systems increasing the energy of the beam before being injected in the LHC. The beam begins in Linac2 and is injected into PS via PSB (written as Booster in the image). The beam is then injected in SPS after PS and is finally injected in LHC. (Image courtesy of CERN)

SPS is the last destination before injected into LHC with an energy of 450 GeV. The beam is split into two beams and sent in opposite directions around the ring of LHC in well-defined bunches. Each beam consists of 2808 bunches with about 10^{11} protons per bunch.

The maximum energy for LHC is 7 TeV per beam which gives a theoretical maximum of 14 TeV when colliding the two beams. However, the highest energy reached at the LHC to date is 13 TeV, in May 2015. The ring, as it sometimes is called, is actually not a perfect circle, it is divided in eight arcs as shown in figure 3.3. The two beams can collide in four places which are the locations of the four main detectors at LHC; ATLAS, ALICE, CMS, and LHCb [27].

3.1.1 Detectors at LHC

The collisions at LHC are studied in the experiments; ALICE, ATLAS, CMS and LHCb, as mentioned above, and are installed in four underground caverns built around the four collision points of the LHC.

- ALICE, an acronym for A Large Ion Collision Experiment, specialises in lead-ion collisions. The state of matter right after the Big Bang is studied here by creating quark gluon plasma.
- LHCb, where b stands for beauty, another name for the bottom quark. It records decays of particles containing b and anti-b quarks, which is partly made to explain the matter and anti-matter asymmetry in the universe.
- CMS, the Compact Muon Solenoid, is designed to investigate a wide range of high energy physics.
- ALTAS, stands for A Toroidal LHC ApparatuS, is located at the other side of the ring from CMS and is designed for similar purposes.

CMS and ATLAS are the two collaborations investigating the properties of the Higgs boson and are made to complement each other. This thesis will focus more on the research done with the ATLAS collaboration.

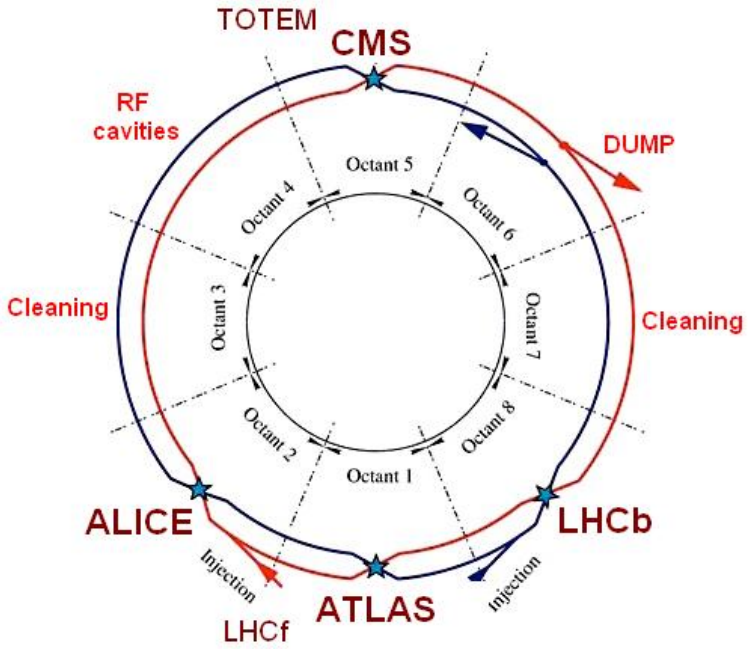

Figure 3.3: View of the LHC divided in eight arcs. ATLAS and CMS are placed at opposite sides of the ring whereas the other two experiments, ALICE and LHCb, are placed on each side of ATLAS. (Image courtesy of CERN)

3.1.2 Luminosity

Luminosity is a central concept in the field of accelerator physics and is a measure of how bright a collider is. $\mathcal{L}$ is called instantaneous luminosity and measures how much data that is produced per unit time. It has the dimension inverse area per unit time: $\mathrm{cm}^{-2}\mathrm{s}^{-1}$.

The instantaneous luminosity of an accelerator is an indication of its performance. Higher luminosity means more collisions per unit time. In order to get the total amount of data the luminosity is integrated over time and is logically called the integrated luminosity.

$$L = \int \mathcal{L} dt \tag{3.1}$$

The number of events for process A, N_A, during a period of time is depending on the probability of the process, i.e. the cross section σ_A, and the total amount of collisions during the same time period, i.e. the integrated luminosity, L. The cross section will in turn depend on the centre-of-mass energy, $\sqrt{s}$, of the accelerator.

$$N_A = \sigma_A \cdot \int \mathcal{L} dt = \sigma_A \cdot L \tag{3.2}$$

LHC is designed with a capacity of 10^{34} $\mathrm{cm}^{-2}\mathrm{s}^{-1}$ for its instantaneous luminosity. Figure 3.4 (a) and figure 3.4 (b) shows the total integrated luminosity as a function of time that was measured in 2011 and 2012 with $\sqrt{s} = 7$ TeV and $\sqrt{s} = 8$ TeV respectively.

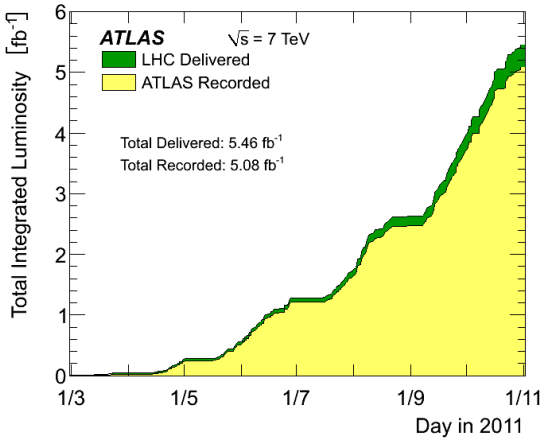

(a) Integrated luminosity by LHC with 7 TeV

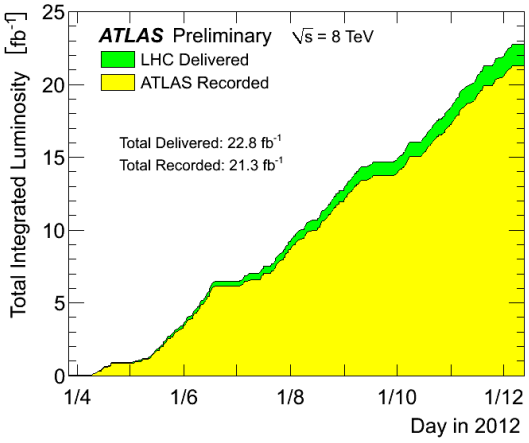

(b) Integrated luminosity by LHC with 8 TeV

Figure 3.4: The integrated luminosity delivered by LHC (green area) and recorded data by ATLAS (yellow) during 2011 with 7 TeV centre-of-mass collision in (a) and during 2012 with 8 TeV centre-of-mass collision in (b). Figure credit [28].

With approximately 20 collisions per bunch crossing every 25 ns, about 1 billion collisions is happening every second. This puts a lot of pressure on the trigger system of the detector to be able to make fast decisions and choose which data to be used in further analysis. Example of this is described below in the trigger system of the ATLAS detector [29].

3.2 ATLAS

ATLAS is a multi-purpose particle detector at LHC shown in figure 3.5. It it 44 m in length and has a diameter of 25 m, making it the largest volume particle detector ever constructed.

Being multi-purpose it can detect and reconstruct almost all particles in the Standard Model. However, neutrinos does not leave any track in the detector except for missing transverse energy.

In order to cover all the different particles, the detector is divided into three major components. Closest to the beam pipe is the inner detector measuring the momentum of each charged particle. Surrounding the inner detector is the calorimeters used to measure the energies carried by the particles. Outermost is the muon spectrometer that identifies muons and measure their momenta [30][31].

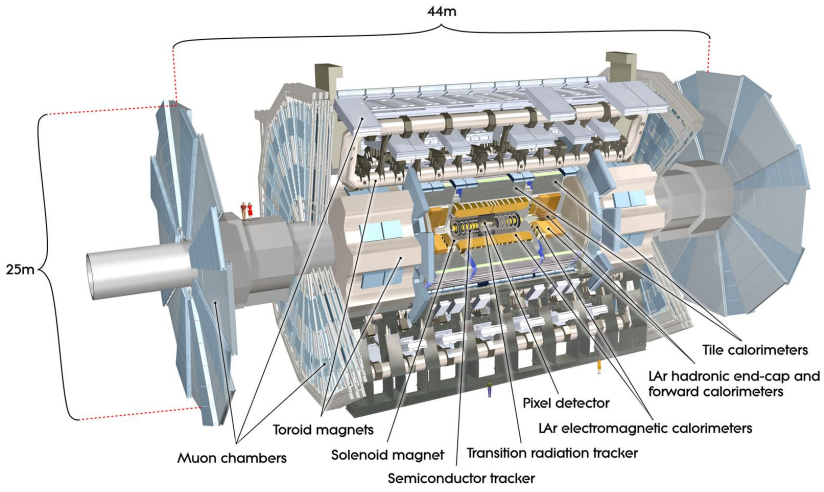

Figure 3.5: Detailed image of the ATLAS detector and its segments with the inner detector, the calorimeters, and the muon spectrometers. (Image courtesy of the ATLAS collaboration)

3.2.1 Coordinate system

The coordinate system of the ATLAS detector is a right handed cylindrical system with its origin in the point of interaction. The z-axis is defined as the direction of the beam along the tunnel. The x-axis is pointing towards the center of the LHC-ring and the y-axis is pointing up towards the surface of the earth.

The azimuthal angle in the transverse plane around the beam is defined as:

$$\phi = \arctan\left(\frac{x}{y}\right) \tag{3.3}$$

The polar angle, θ, measuring from the z-axis to the direction of the particle, is parametrised as the pseudorapidity, η.

$$\eta = -\ln\tan\left(\frac{\theta}{2}\right) \tag{3.4}$$

Small values of the pseudorapidity indicates direction of the scattering to be close to orthogonal to the beam pipe, whereas larger values indicates the direction to be along the beam pipe. The different angles for the pseudorapidity are shown in figure 3.6.

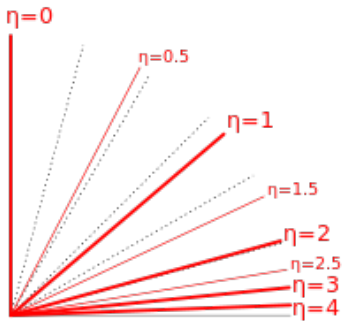

Figure 3.6: Values of pseudorapidity where $\eta = 0$ is at 90 and higher values of η are quickly approaching the direction of the beam pipe for $\eta > 2$. Figure credit [32].

3.2.2 Inner Detector

The inner detector covers $|\eta| < 2.5$ and is contained in a solenoid which provides a nominal magnetic field of 2 T. The purpose of the inner detector is to measure the momentum and direction of charged particles created in the collision. It begins a few centimeters from the proton beam, has an outer radius of 1.15 m and is 7 m long along the beam pipe.

It consists of three subsystems with complementary properties; a pixel detector, a semi-conductor tracker (SCT) and a transition radiation tracker (TRT). A cut-away view of the inner detector in ATLAS can be seen in figure 3.7.

Closest to the beam pipe is the pixel detector consisting of three[1] concentric barrels and three disks at each end cap. It is designed for high spatial resolution and precision measurements giving the pixel detector the ability to make a distinction between primary and secondary vertices. This is to identify short-lived particles, such as b-hadrons, that travels a short distance in the detector before further decay creating a second vertex.

The middle component of the inner detector is the semi-conductor tracker. It covers a larger area than the pixel detector and provides eight precise measurements for each track. This contributes to the ability of the inner detector to measure momentum, impact parameters and vertex positions.

The outer most layer is the transition radiation tracker and is based on a combination of a radiation detector and a gaseous straw tracker. It is, as the other two above, made up by a barrel part and end cap parts. The uncertainty of the TRT is not as precise as the other two systems in the inner detector, but it covers a greater area in the barrel which would be too expensive with semi-conductors. The straws are parallell to the beam and the gas in them will get ionised when charged particles are passing through, which is used for particle identification.

[1]This is true for the construction of ATLAS used in run 1 when the data used in this thesis was collected. However, a new layer between the beam pipe and pixel detector called IBL (Insertable B-Layer) was installed in 2014 as part of the upgrade for run 2 starting in 2015.

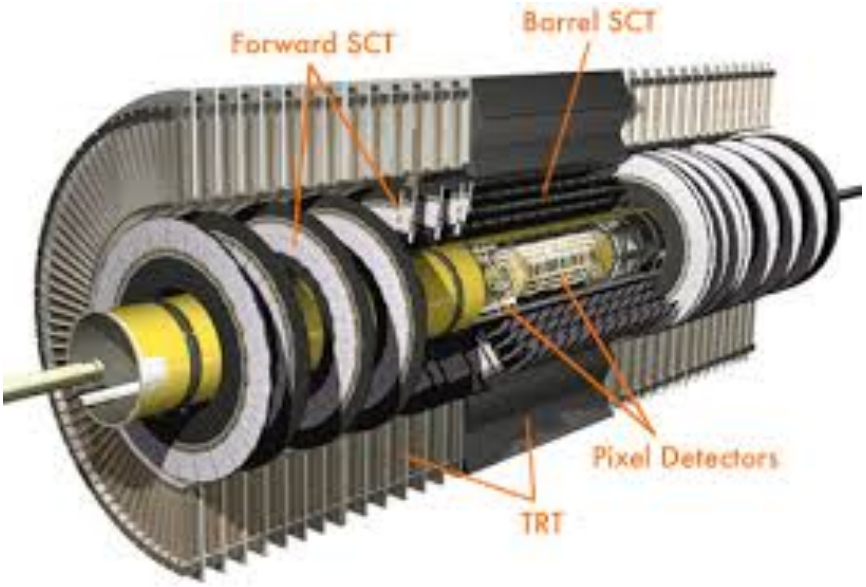

Figure 3.7: Cut-view of the inner detector of ATLAS and its segments with the pixel detectors, the semi-conductor trackers, and the transition radiation trackers. (Image courtesy of the ATLAS collaboration)

3.2.3 Calorimeter

Further identification of particles after the inner detector is made in the calorimeter with the purpose of measuring the energy of charged and neutral particles. The calorimeter in ATLAS is divided in two sub-detectors; the electromagnetic calorimeter (E-Cal) and the hadronic calorimeter (H-Cal), as seen in figure 3.8.

When a particle passes through the calorimetries it interacts with the dense material creating cascades of secondary particles called showers. The electromagnetic showers of electrons and photons are generally shorter and more narrow than the hadronic showers that are mainly consisting of pions.

Since particles with high mass, such as the hadrons, tend to propagate to a greater depth in the detector than light particles like electrons and protons, the electromagnetic calorimeter is placed closest to the inner detector with the hadronic calorimeter on the outside. Both are so called sampling calorimeters consisting of absorbing material, that initiates the particles to create showers, and sampling material, that is measuring the energy deposited. By layering the absorbing and sampling materials, the total energy of the propagating particle can be calculated.

The electromagnetic calorimeter is used to measure the energy from electrons and photons. It consists of layers of lead and stainless steel as absorption material and liquid argon as sampling material. When particles interact with the absorbing materials a shower of new electrons is produced which is detected by the liquid argon.

The hadronic calorimeter is used to measure the energy of hadronic particles, mainly protons, neutrons and mesons. Steel works as absorption material and sampling is made by scintillating plastic tiles. Showers in the hadronic calorimeter makes the plastic tiles to emit light which is then detected by photomultiplying tubes (PMTs).

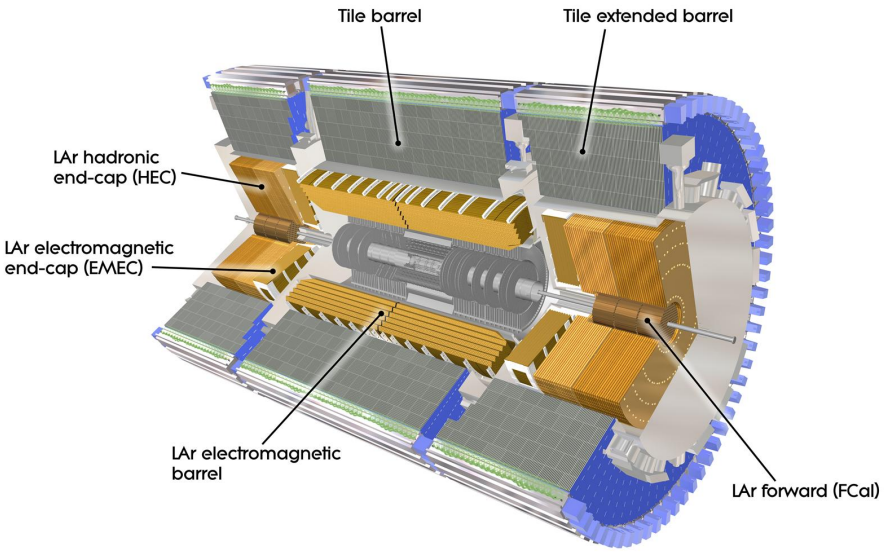

Figure 3.8: Cut-view of the calorimeters of ATLAS with the segments of the electromagnetic calorimeter and the segments of the hadronic calorimeter. (Image courtesy of the ATLAS collaboration)

There is also a part of the calorimeter in ATLAS called the forward calorimeter (F-Cal). It is used to cover particles in the forward direction of the detector, that is, particle showers close to the direction of the beam pipe. F-Cal uses tungsten as absorbers and liquid argon as sampling material as in E-Cal.

The calorimeters in ATLAS are designed in such a way that the only particles passing through should be muons and neutrinos.

3.2.4 Muon Spectrometer

Muons are a heavier cousin to the electron and are highly penetrating making them the only particles (except neutrinos) to reach outside the calorimeters. ATLAS is therefore using a muon spectrometer surrounding the calorimeters. The muon spectrometer is designed with two main functions; the trigger chamber, to rapidly identify muons, and the tracking chamber, to measure the momenta of the muons. A cut-view of the muon spectrometer can be seen in figure 3.9.

The trigger chamber in turn consist of resistive-plate-chambers (RPC) around the barrel of the detector and thin-gap-chambers (TGC) by the end caps.

The tracker of the muon spectrometer has a function similar to the straws in the inner detector but is larger in size leading to lower spatial resolution. Magnetic field bends the muon tracks, and their momenta can then be determined by measuring the curve of the track. As in the trigger chamber, the tracker has also two different types in order to detect muons in all directions. The subsystems consists of monitor drift tubes (MDTs) and cathode strip chambers (CSCs). MDTs are gas-filled straws located on both the barrel and on the disks by the end caps. CSCs are straws radially aligned from the beam pipe by the end caps.

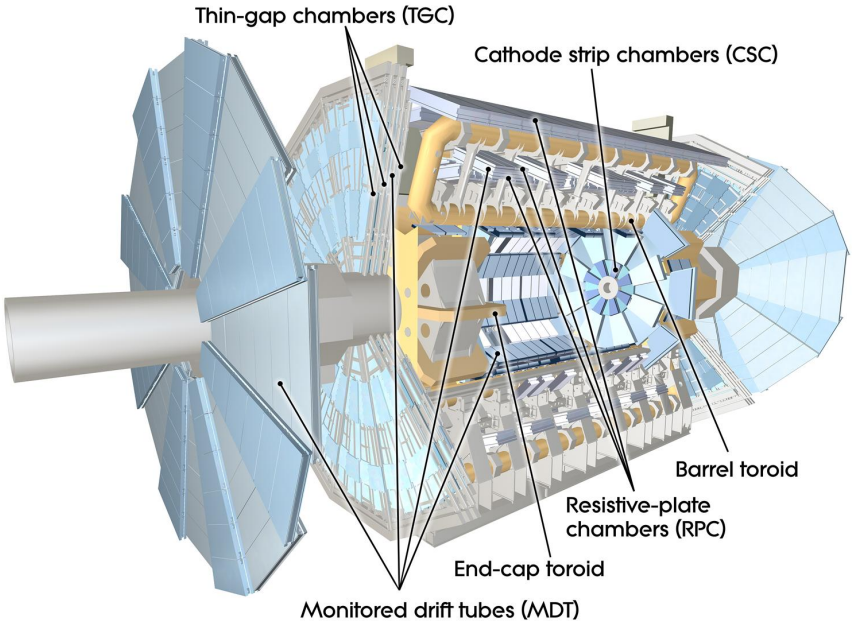

Figure 3.9: Cut-view of the muon spectrometer of ATLAS and its segments with the trigger chamber and the tracking chamber. (Image courtesy of the ATLAS collaboration)

3.2.5 The Trigger System

About one billion collisions is happening in ATLAS every second generating too much unnecessary data to manage. The trigger system is therefore an essential part of the detector. The trigger system of ATLAS is divided into three levels; level-1, level-2, and the event filter.

Level-1 is based in the electronics of the detector using information from the calorimeters and the muon spectrometer. The level-1 trigger has about 2 μs to reach a decision on which events to keep and selects about 100.000 events per second to send to the next level.

The other two levels of triggers are both run on computer clusters positioned near the detector. Level-2 has up to 40 ms to reach a decision which gives it more time for calculations using information from all detectors on the events picked by level-1.

The last filter, the event filter, has about 4 s to refine the selection of events. A couple of hundred events per second is finally selected for offline storage and used in further analysis.

3.3 Particle Identification

The ATLAS detector is constructed in such a way to be able to identify all particles in the Standard Model described in section 2.1. The magnetic field in the inner detector bends the trajectories of charged particles making it possible to measure their momenta.

Single quarks are not possible to detect since they cannot be in a free state, they are detected as different hadrons instead. Hadronisation of quarks creates so called jets, identified as cone-shaped showers in the calorimeter. A schematic overview of the tracks in the different detector parts can be seen in figure 3.10.

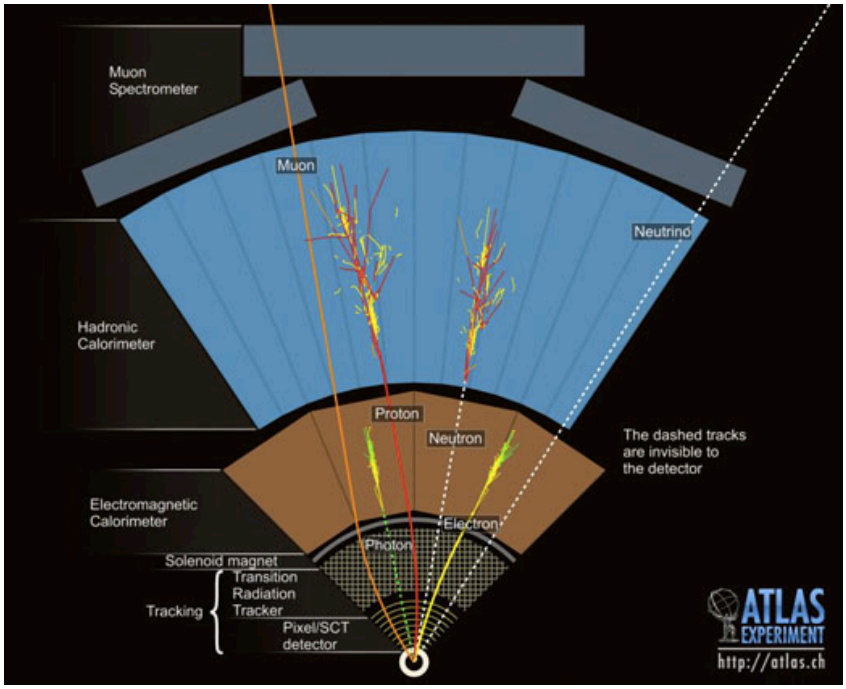

Figure 3.10: Schematic overview of how the different detector parts of ATLAS will give rise to signals depending on the particle and how this is used in particle identification. (Image courtesy of the ATLAS collaboration)

An overview of how the identification signal for Standard Model particles looks like can be seen in figure 3.11.

Photons have no electric charge and will therefore not leave a track in the inner detector. It will deposit all its energy in the EM calorimeter.

Electrons and positrons will leave a track in the inner detector since they are charged particles and then, as the photon, deposit its energy in the EM calorimeter.

Muons are also charged and will leave a track in the inner detector but cannot be stopped in the calorimeters because it does not interact strongly. It will instead deposit a little bit of energy in both the EM and the hadronic calorimeters and finally leave a track in the muon spectrometer.

Charged hadrons, such as charged pions and protons, will leave a track in the inner detector because of its electric charge. It will then deposit some energy in the EM-calorimeter but deposit most of its energy in the hadronic calorimeter.

Neutral hadrons, such as the neutral pion of the neutron, leave no track in the inner detector. It will as the charged hadron, deposit some energy in the EM-calorimeter but most of it in the hadronic calorimeter.

Neutrinos is the only particle that is not detected in the ATLAS detector. It is instead identified as missing transverse momentum, usually denoted by missing E_T or E_T^{miss}. This is because when the proton beams collide they only have initial momentum in z-direction. The sum of the momentum in the transverse plane should therefore be zero.

Heavier particles than those describes above will decay at once and their decay particles are the ones detected instead. The initial particles can then be identified by analysing the final state of the decay particles.

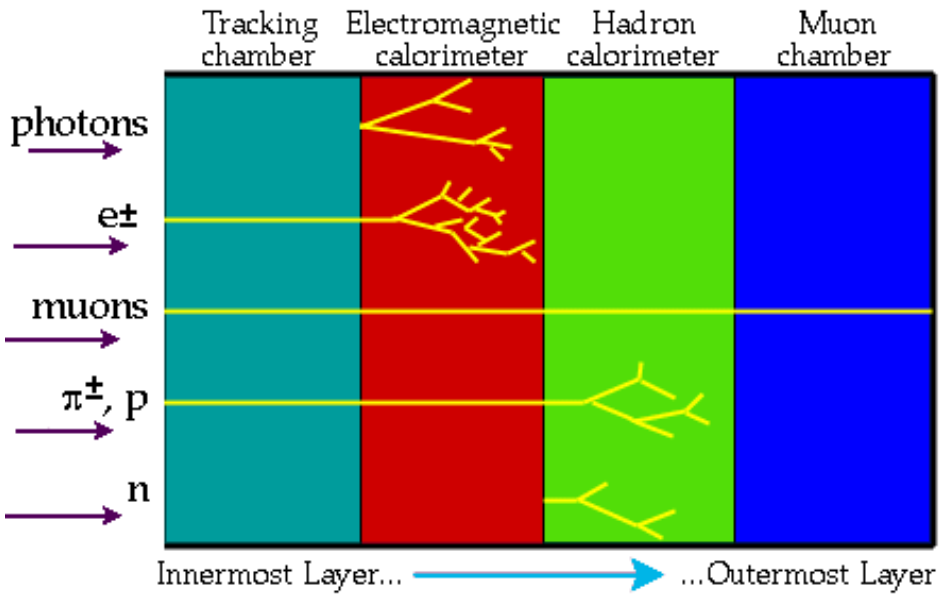

Figure 3.11: Overview of identification of particles by their tracks in the different detectors from inner part to the outer part of the layers of the ATLAS detector. (Image courtesy of the ATLAS collaboration)

Chapter 4

The Higgs Boson Phenomenology

One of the main tasks for the ATLAS and CMS experiments at LHC is to detect the Higgs boson and investigate its properties.

The Higgs boson itself cannot be detected due to the fact that it decays immediately. Identification of the Higgs boson is thus made by analysing its decay particles. The signal from a Higgs event in the analysis will depend on the production as well as the decay. The production of the Higgs boson can occur in various processes when two proton beams collide. In this chapter the product and decay channels with the highest cross section will be discussed [3].

4.1 Production Channels

The Higgs boson can be produced in the LHC by proton-proton collision in different processes called production channels. The cross section for a production channel, seen in figure 4.1, depends on the coupling of the process and the mass of the Higgs boson. While the Higgs boson couple to massive particles proportional to the mass of a particle, it couples proportional to the mass squared for gauge bosons. The four leading processes is described below in order of highest to lowest cross section [33].

The gluon-gluon-fusion production channel, **ggF**, is the dominating process for the Higgs boson. It is mainly the one used in the Higgs analysis and is shown in figure 4.2. Since gluons are massless they cannot couple directly with the Higgs boson but couple via a quark-loop instead. The top quark is the heaviest quark and therefore the one to couple strongest with the Higgs boson.

The second leading process is vector boson fusion, **VBF**, where the vector bosons are either W or Z bosons. As can be seen by the Feynman diagram in figure 4.3, two quarks each radiates a vector boson which annihilates producing a Higgs boson. This process will also result in creating two high energetic jets opposite each other along the beam pipe.

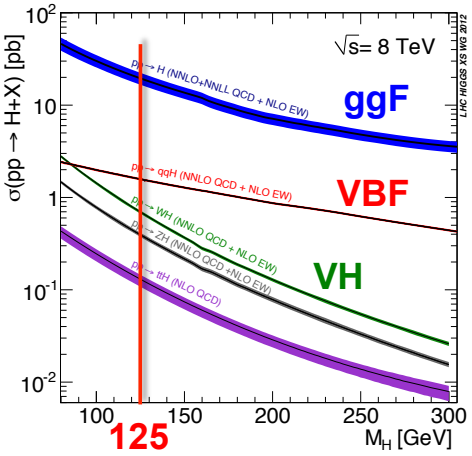

Figure 4.1: Cross section of the leading Higgs production channels in proton-proton collision as a function of the Higgs mass. The known Higgs mass of 125 GeV is marked by the red line. Figure credit [34].

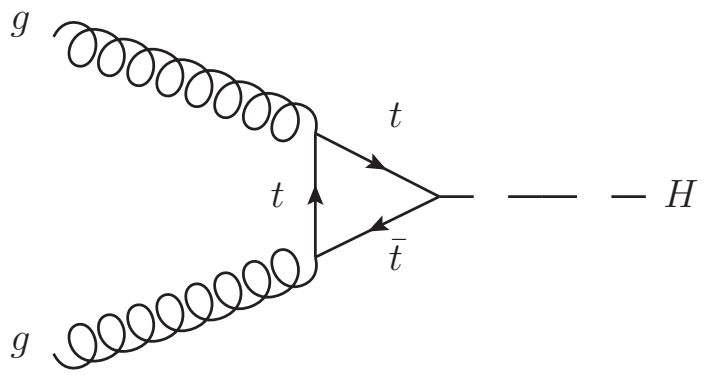

Figure 4.2: Feynman diagram of the ggF-production channel with two gluons couppeling to the Higgs boson via a top-quark loop. This has a cross section of σ=19.3 pb for Higgs mass 125 GeV.

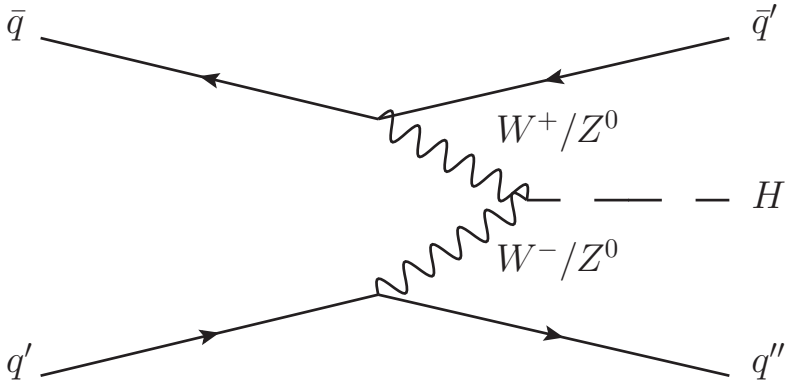

Figure 4.3: Feynman diagram of the VBF production channel with two quarks each radiating vector bosons which annihilates producing a Higgs boson. This has a cross section of σ=1.6 pb for Higgs mass 125 GeV.

W/Z-bremsstrahlung is a so called "associated production", denoted **VH**, and the third leading production channel. Seen in figure 4.4, quark and anti-quark annihilates producing a virtual vector boson, W or Z, which in turn decays into a real vector boson and a Higgs boson.

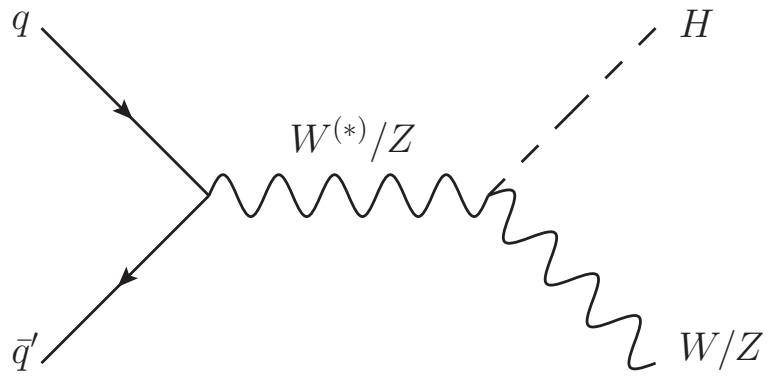

Figure 4.4: Feynman diagram of the VH production channel where two quarks annihilates producing a virtual vector boson which in turn produces a real vector boson and a Higgs boson. This has a cross section of σ_W=0.7 pb for W and σ_Z=0.42 pb for Z, for Higgs mass 125 GeV.

The last of the four leading production channels is quark-quark-fusion displayed with top quarks in figure 4.5. As seen in the Feynman diagram quark and anti-quark, produced by gluons, annihilates producing a Higgs boson. Once again, since the top quark is the heaviest quark, it will couple strongest with the Higgs boson and is therefore the dominant process, denoted **ttH**.

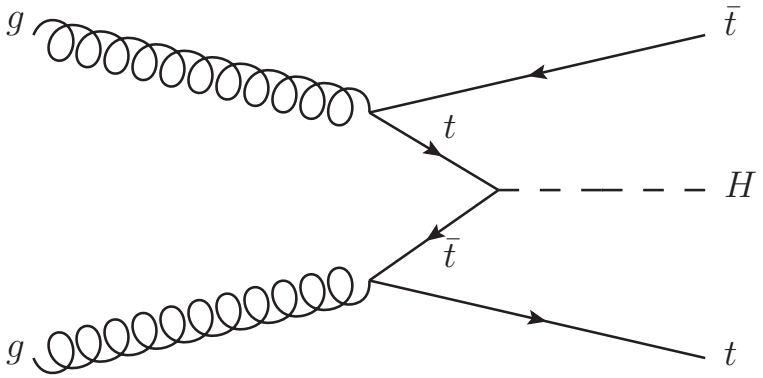

Figure 4.5: Feynman diagram displaying ttH production channel where gluons radiates a pair of quark antiquark pair of top quarks which in turn annihilates producing Higgs. This has a cross section of σ=0.13 pb for Higgs mass 125 GeV.

These last two production channels are not used in the Higgs analysis due to its low cross section in comparison to the dominating gluon-gluon-fusion, ggF. One of the goals for run 2 at LHC, which began in May 2015, is to use ttH production in the analysis.

4.2 Decay Channels

Even though the Higgs boson in general couples strongest to heavy particles, like the top quark, W and Z bosons, it is most likely to decay into particles with combined mass lower than the Higgs mass itself. For the Higgs mass 125 GeV the highest branching ratio is the decay channel of two bottom quarks. The branching ratio is the frequency of a particular decay mode relative to the total number of decay modes. It is a way of describing the probability of particle decay and is shown in figure 4.6 for the different decay channels [35].

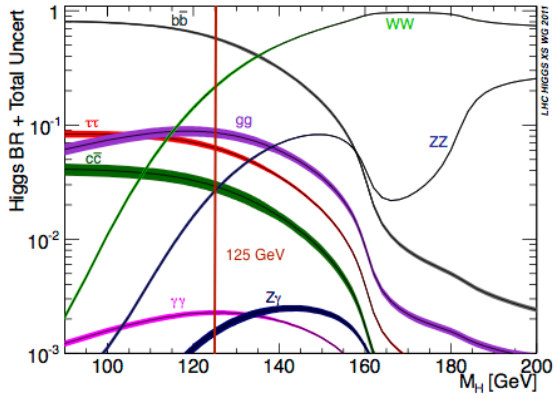

Figure 4.6: Branching ratio of Higgs decay channels as a function of the Higgs mass, where the known Higgs mass of 125 GeV is marked by the red line. Figure credit [34].

The highest branching ratio is, as written above, the Higgs decaying into two bottom quarks which is shown in figure 4.7. Despite it having the highest branching ratio, it is not a good channel to use in the Higgs analysis due to the difficulty of distinguishing the Higgs events from backgrounds where similar jets are produced.

The decay channel used in the Higgs analysis is, because of this, not necessarily the ones with the highest branching ratio. What is more important is rather decay channels with final states that are easy to distinguish from the backgrounds with similar final states. The decay channels used in the Higgs analysis at the ATLAS and CMS experiments are therefore the WW, ZZ, and $\gamma\gamma$ decay channels.

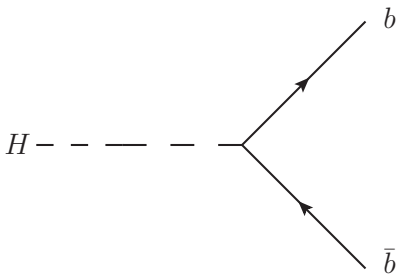

Figure 4.7: Feynman diagram of the decay mode where the Higgs boson decays into two bottom quarks. This is the decay mode with highest branching ratio at the Higgs mass of 125 GeV.

The decay channel used in this thesis is the WW channel. At Higgs mass of 125 GeV, the branching ratio of the WW channel is the highest after the bb-channel. However, the W bosons cannot be detected themselves since they immediately decay into new particles. The cleanest mode used in the analysis is WW decaying into two charged leptons and two neutrinos as shown in figure 4.8. This is not the most probable decay mode, resulting in lower branching ratio. The charged leptons are easy to identify though and gives a clean final state with still relatively high branching ratio. A drawback with this decay mode is that neutrinos cannot be detected in ATLAS or CMS and are identified only as missing transverse momentum, which makes it impossible to reconstruct the Higgs mass completely.

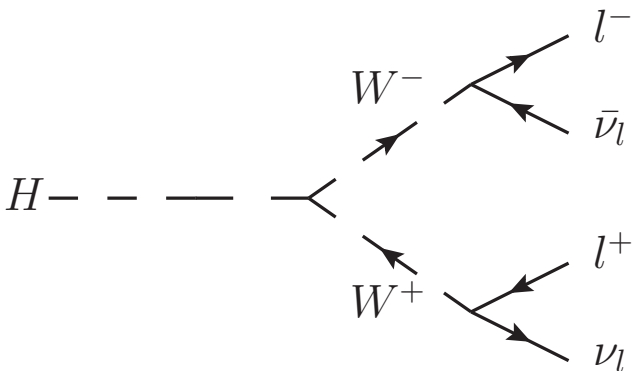

Figure 4.8: Feynman diagram of the WW decay mode where the Higgs boson decays into two W-bosons which in turn have the final stare of $l^-\bar{\nu}_l l^+\nu_l$ used in the Higgs analysis.

Another decay channel used in the Higgs analysis is where the Higgs boson decay into two Z bosons. These can in turn decay into four charged leptons as seen in figure 4.9. This has a very low branching ratio but is a clean mode with the Higgs events being easy to distinguish from the background. Compared to the WW-channel, the ZZ-channel can, with its final state of four charged leptons, completely reconstruct the Higgs mass.

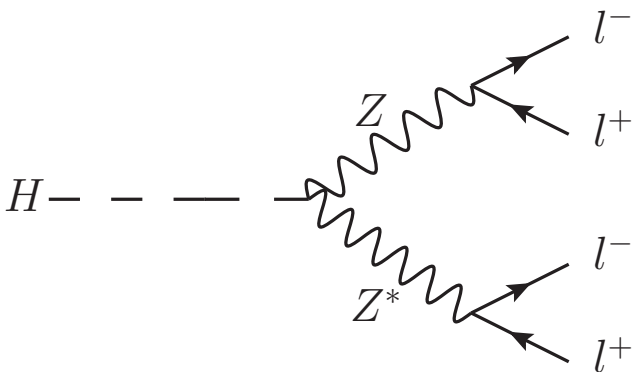

Figure 4.9: Feynman diagram of the decay mode where the Higgs boson decays into two Z-bosons with the final state of $l^+l^-l^+l^-$ used in the Higgs analysis.

The $\gamma\gamma$-channel has a fairly low branching ratio due to the fact that the massless photons cannot couple directly with the Higgs boson as seen in figure 4.10. Despite this, it is still a very interesting channel to be used in the Higgs analysis because of it being a clean channel and easy to distinguish. The two photons can furthermore, as in the ZZ-channel, be completely reconstructed and will give a good measurement of the Higgs mass.

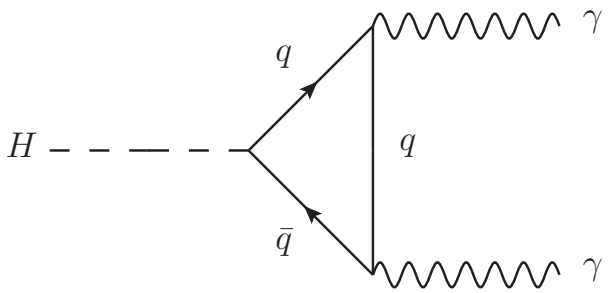

Figure 4.10: Feynman diagram of the decay mode where the Higgs boson decays into two photons via a quark loop used in the Higgs analysis

In order to get the total cross section, that is the actual amount of the Higgs events for the different processes, both the cross section of the production and branching ratio of the decay modes need to be taken into account. The total cross section of the different Higgs decay channels is thus the product of the production cross section and the branching ratio of the different modes, which is shown in figure 4.11 [36].

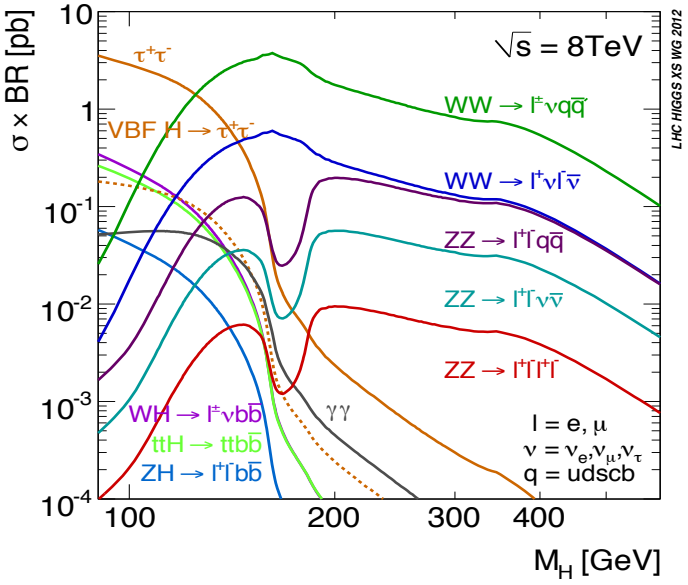

Figure 4.11: The total cross section of the Higgs events decaying into certain modes calculated as the product of production cross section times the branching ratio. Figure credit [34].

Chapter 5

Analysis of $H \rightarrow WW^*$

On 4th of July 2012, the ATLAS and CMS Collaborations announced the discovery of a Higgs like boson at mass 125 GeV [37]. One of the decay channels used in the analysis supporting the announcement was $H \rightarrow WW^* \rightarrow l\nu l\nu$. This is the decay of the Higgs boson to two W-bosons which immediately decays into two leptons and two corresponding lepton neutrinos. It is one of the cleanest decay modes of the Higgs boson, but has the drawback of not being able to completely reconstruct the mass of the final state particles because of the neutrinos. Further explanations of this and what it means for the analysis will be discussed in this chapter [5].

5.1 The Signature of WW*

The mass of the Higgs boson is determined to be 125 GeV which is lighter than the mass of two W-bosons (since mass of a W-boson is 80 GeV). This means that in the decay mode of $H \rightarrow WW^*$, one of the W-bosons will be virtual, denoted W^*.

The decay mode of $H \rightarrow WW^* \rightarrow l\nu l\nu$ is a clean decay mode with its two isolated oppositely charged leptons and neutrinos as final particles. The leptons used in the analysis of this mode are electron and muons since the τ-lepton is very unstable due to its heavy mass. The two leptons can either be of the same flavour (ee or $\mu\mu$), SF, or different flavour ($e\mu$ or μe), DF.

Because of the high E_T^{miss}, it is not possible to completely reconstruct the invariant mass of the Higgs boson in this decay mode. The transverse mass is instead used and defined as:

$$m_T = \sqrt{(E_T^{ll} + E_T^{miss})^2 - |\bar{p}_T^{ll} + \bar{E}_T^{miss}|^2} \tag{5.1}$$

where: $E_T^{ll} = \sqrt{|\bar{p}_T^{ll}|^2 + m_{ll}^2}$.

The Higgs boson is mainly created via ggF and VBF, as discussed in chapter 4. Depending on the production mode, the final state particles will be different, as can be seen by the Feynman diagrams in figure 5.1. In VBF-production, there will also be two high energetic jets along the beam pipe, which is not the case in ggF.

In all production modes, the leading lepton in this decay mode will have high transverse momentum, P_T. This is because only one of the W-bosons is real, whereas the other one is virtual.

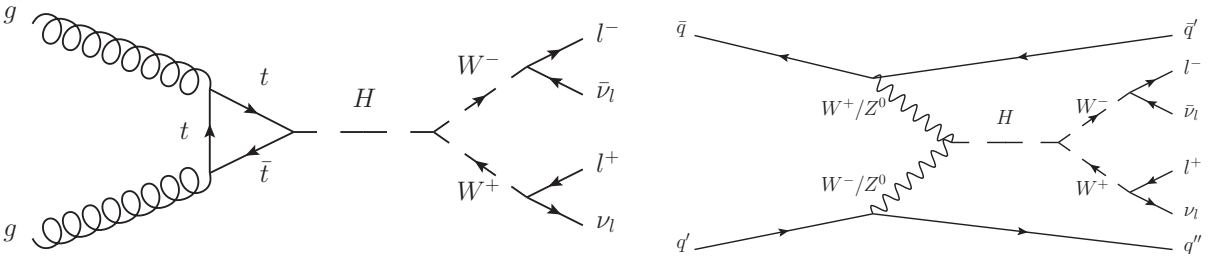

(a) Production to decay with ggF *(b) Production to decay with VBF*

Figure 5.1: Feynman diagram with Higgs decaying into WW with prodcution channels: (a) ggF, with two leptons and two neutrinos as final particles, and (b) VBF, with two leptons, two neutrinos, and two quarks as final particles.

The Higgs boson has Spin-0, which will affect the direction of the leptons in the transverse plane of the detector, as seen in figure 5.2. In order to conserve angular momentum, the W-bosons have to be anti-aligned since W-bosons have spin-1. Because of V-A coupling, the weak force only couples to left-handed leptons, making the two leptons propagate in the same direction with the two neutrinos in opposite direction of the leptons. This will give a signal in the detector, as in figure 5.3, with two leptons in the same direction and high missing transverse energy, MET or E_T^{miss}, in the opposite direction. The Standard Model produced WW background do not have the same spin correlation as the Higgs produced W bosons, which means that the background signal rarely have leptons propagating in the same direction [38].

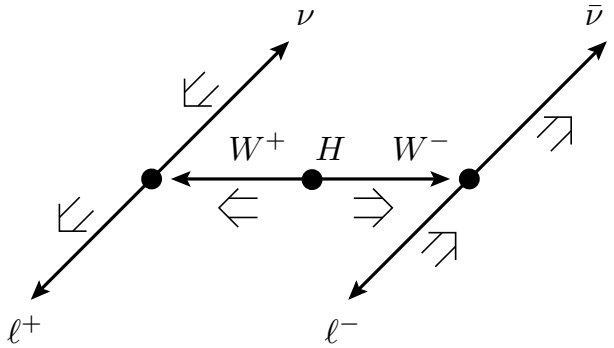

Figure 5.2: Illustration of how the spin-0 Higgs boson decays to two W-bosons with opposite spin. The spin-1 W bosons then decay into leptons with aligned spin. The small arrows indicate the propagating direction of the particles and the large arrows their spin projection. Figure credit [5].

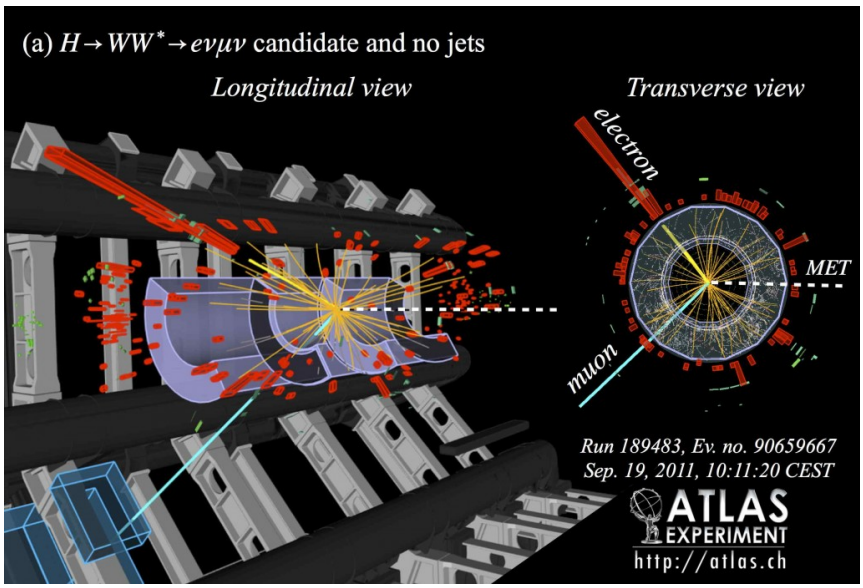

Figure 5.3: $H \to WW \to l\nu l\nu$ event and how the signal looks like in the ATLAS detector, where the left side of the figure displays a Higgs signal event in the longitudinal view of the detector and the right side displays the transverse plane. The thick yellow line is an identified electron, the thin light blue line is an identified muon and the black-and-white dashed line is missing transverse energy which is probably due to neutrinos. Figure credit [39].

5.2 Backgrounds

There are processes other than $H \to WW \to l\nu l\nu$ that can give rise to the same set of final particles. These are called background events to the $H \to WW$ decay channel. Backgrounds in this sense can also be processes creating final particles that are misidentified as leptons or neutrinos. The misidentified particles are called "fake" particles. The relevant backgrounds to the Higgs analysis will be described in this section. The distinguishing properties of these backgrounds is the motivation for the categories of leptonic flavour and jet multiplicity in the event selection (discussed in section 5.4).

5.2.1 Standard Model WW background

The SM WW background is the dominating background in the category of different leptonic flavour events with no detected jets. It is the most important background for this thesis and is characterised by two leptons that are well separated and two corresponding neutrinos. This background has the same final particles as a Higgs event with the difference that there are no spin correlations in the SM production. There is therefore nothing forcing the leptons to propagate in the same direction as there is in a Higgs event. In fact, it is more favourable for the leptons to propagate in opposite direction of each other. The SM WW background can, with this, be reduced using constraints on the topology of the two leptons such as the angle between them. The Feynman diagram of SM WW production and decay into two leptons and two neutrinos can be seen in figure 5.4.

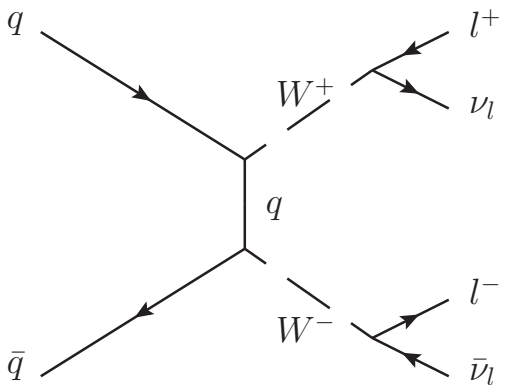

Figure 5.4: Feynman diagram of the Standard Model WW background where two produced W bosons give the same set of final particles with two leptons and two neutrinos as a $H \to WW \to \nu l \nu l$ event.

5.2.2 Top background

A pair of top quarks can also be the source of two pairs of leptons and neutrinos but is accompanied by b-quarks as well, which can be seen in figure 5.5. The top quark is the heaviest fermion in the SM and will decay into a W boson and a b-quark almost every time. The leptonic decay of the W bosons make the background look similar to a $H \to WW \to l\nu l\nu$ event except for the addition of two high momentum jets.

Because b quarks have a relatively long lifetime, they will travel a short distance in the detector before further decay. The result of a secondary vertex identified in the inner detector is a process called "b-tagging". This distinguishes the top background from real Higgs events which rarely contain jets originating from b-quarks. However, the "b-tagging" identification algorithm is rather inefficient, leading the top background to give a significant contribution to the total background for events with one or more identified jets.

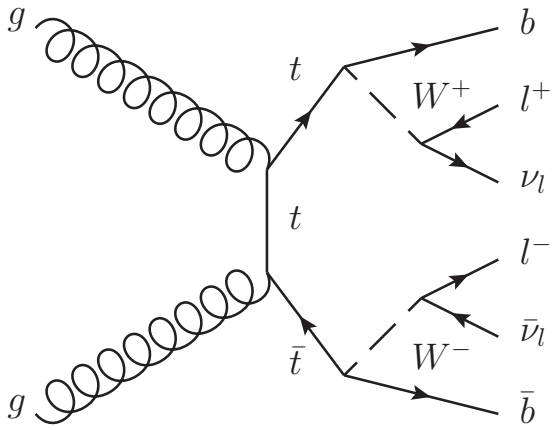

Figure 5.5: Feynman diagram of the top background where two top quarks decay into pairs of b quarks and W bosons giving final particles of a $H \to WW \to l\nu l\nu$ event with two leptons and two quarks as well as the two b quarks.

5.2.3 $W+$ jets Background

Collisions producing W bosons together with jets may give the same signal as a $H \rightarrow WW \rightarrow l\nu l\nu$ event if misidentified. A low energetic jet can actually be wrongfully reconstructed as a lepton, called a "fake leptons". The final particles in the detector will then be two leptons and missing transverse energy from the neutrino as seen in figure 5.6.

The two reconstructed leptons can either be same or oppositely charged to one another, whereas the two leptons in a Higgs event are always of opposite charge. The fake lepton is also usually occurring together with other identified particles, which is not the case in a real Higgs event. To suppress this background an important cut is therefore the requirement of two isolated oppositely charged leptons.

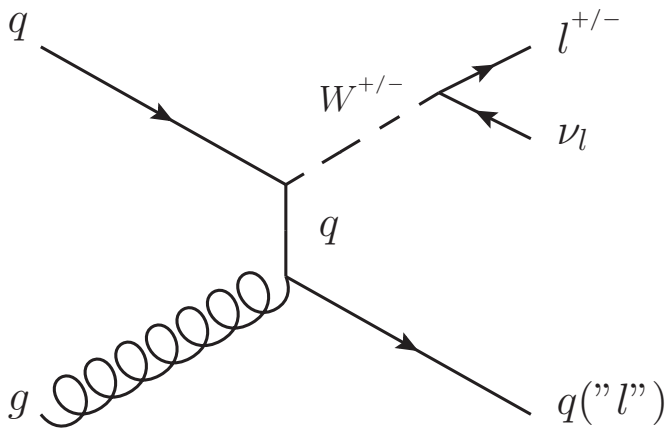

Figure 5.6: Feynman diagram of the W + jet background where a jet is misidentified as a lepton in the detector giving the signal of two leptons and missing transverse energy from the neutrino looking like a $H \rightarrow WW \rightarrow l\nu l\nu$ event.

5.2.4 Drell-Yan Background

Drell Yan background is the name for when Z-bosons or virtual photons decay into a pair of electrons, muons, or tau-leptons. When the lepton pair in the Drell Yan background are electrons or muons, it will be very similar to the signal of a real Higgs event. Even though this process does not contain any neutrinos, as seen in figure 5.7, E_T^{miss} can still be reconstructed and misidentified as fake neutrinos. This process has high cross section, making it an important background in the analysis. But because of lepton number conservation, the two leptons need to be of the same flavour, which is not always the case in WW decay. The two leptons in $WW \rightarrow l\nu l\nu$ can either be of the same flavour or different, which is why the events are divided in leptonic flavour categories in the analysis.

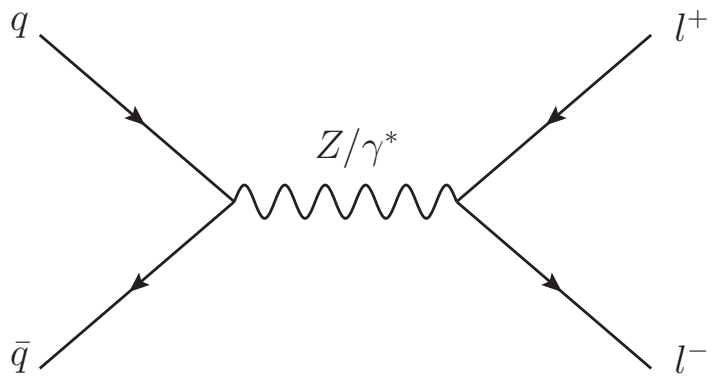

Figure 5.7: Feynman diagram of the Drell Yan background with two leptons of the same flavour as its final particles.

The tau-leptons in a Drell-Yan background will quickly decay into new particles. As seen in figure 5.8 this can give the decay product of two leptons, being electrons or muons, and four neutrinos. Since neutrinos are only identified as E_T^{miss} it is hard to distinguish four neutrinos from two. However, this background with two tau-leptons is rare and insignificant in SF events. It is the only contribution from the DY background in DF events though, which is why it still is an important background. The two leptons in this event has very low P_T, making constraints on P_T for the two leptons necessary to suppress this background.

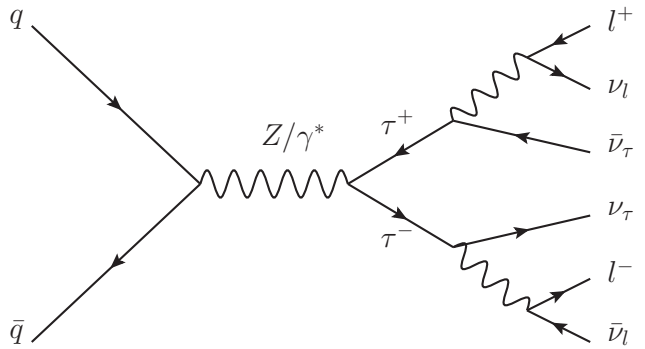

Figure 5.8: Feynman diagram of the Drell Yan background with τ-leptons and final particles of two leptons and four neutrinos identified as E_T^{miss}.

5.3 Analysis Strategy

The cuts made in the event selection is done to suppress as much background as possible. The most important background for this thesis is the SM-WW background since it contains W-bosons decaying into the same set of final particles. Because of its final particles being the same as a real Higgs event it is important to look at the angle between the two leptons in the dilepton system, $\Delta\phi_{ll}$. In a Higgs event both leptons propagates at the same direction because of Higgs having spin-0, which is not the case in the SM-WW background.

The transverse momentum, P_T, on both leptons is also a very important cut. Separation of leading and subleading leptons is done due to the fact that the mass of the Higgs boson is less than the combined mass of two real W-bosons, leading one of the W-boson mass to be off-shell. This makes one of the leptons, the so called subleading lepton, not as energetic as the leading one. By separating the cuts on these two, a higher P_T-cut can be set on the leading lepton since too much signal would be lost with as high P_T cut on the subleading lepton.

The Drell-Yan background is one of the main backgrounds to reject. But Z-bosons decays to same flavour leptons making it useful to separate events with same flavoured lepton events and different flavoured lepton events. In result, different cuts depending on SF and DF events are made which almost eliminates the Drell-Yan background for DF events.

To separate the number of jets in an event is also important. The top background is easiest to eliminate by applying jet veto and b-jet veto cuts, see figure 5.9. Jet veto is in general an effective cut to eliminate background events, however, this also eliminates Higgs events originating from VBF production.

The data collected and reconstructed by ATLAS is compared with predictions made by Monte Carlo Simulations. The more data collected, the lower the statistical uncertainty will be in the analysis. For the simulated events in Monte Carlo the production channels considered in the analysis for the production of Higgs bosons are ggF and VBF production. VH production is also simulated but is negligible in its contribution to the Higgs production. For ggF production, which is the dominating production channel, the predictions are computed up to next-to-next-to-leading order, NNLO.

5.4 Event selection and Cuts

Event selection is the first part of the analysis and consists of a series of cuts made to reduce events originating from the backgrounds described above. It is divided into three parts: pre-selection cuts, jet multiplicity, and topological cuts. Different cuts are applied in these three stages depending on if the two leptons are of SF or DF [5].

5.4.1 Pre-Selection Cuts

The first set of cuts in the event selection are the so called pre-selection cuts. These starts off by requiring an event containing exactly two isolated leptons, oppositely charged, with primary vertex at the collision point. The pre-selection cuts are summarised in table 5.1.

In order to reduce the risk of misidentifying jets as fake leptons the first requirement in the pre-selection is to identify two oppositely charged isolated leptons. Since one of

the W-bosons is virtual assymetric cuts are applied for the two leptons. Limits for P_T is set to $P_T > 22$ GeV for the leading lepton and $P_T > 10$ GeV for the subleading lepton.

A lower limit is set on the invariant mass of the two leptons, $m_{ll} > 10$ GeV for DF leptons and $m_{ll} > 12$ GeV for SF leptons, to reduce the contribution of leptons originating from virtual photons and low mass resonances. A Z-veto cut is also applied for SF events with $|m_{ll} - m_Z| > 15$ GeV to reduce the contribution of leptons originating from Z-bosons.

The last cut of the pre-selection is the requirement of high missing transverse energy, E_T^{miss}, not in the direction of any lepton or jet. Due to this, a refined definition of the missing transverse energy is used in the analysis and given by:

$$E_{T,rel}^{miss} = \begin{cases} E_T^{miss} & \text{if } \Delta\phi \geq \pi/2 \\ E_T^{miss} \cdot \sin(\Delta\phi) & \text{if } \Delta\phi < \pi/2 \end{cases} \tag{5.2}$$

where $\Delta\phi$ is the angle between the direction of E_T^{miss} and the nearest lepton or jet. The limit is used to reduce events with E_T^{miss} in the same direction as the leptons and is set to $E_{T,rel}^{miss} > 20$ GeV for DF leptons and to $E_{T,rel}^{miss} > 40$ GeV for SF leptons.

Table 5.1: Summary of the pre selection cuts

Variables	Cuts
Leptons	Two isolated leptons with opposite sign.
P_T	> 22 GeV for the leading lepton. > 10 GeV for the subleading lepton.
m_{ll}	> 10 GeV for DF leptons. > 12 GeV for SF leptons.
Z-veto	$\|m_{ll} - m_Z\| > 15$ GeV for SF leptons.
$E_{T,rel}^{miss}$	> 20 GeV for DF leptons. > 40 GeV for DF leptons.

5.4.2 Jet-multiplicity

After the pre selection cuts the analysis is divided into three branches depending on the number of jets found in the event: $N_{jet} = 0$, $N_{jet} = 1$, and $N_{jet} \geq 2$. Figure 5.9 displays the different backgrounds divided into bins depending on the jet multiplicity.

The $N_{jet} = 0$ branch, meaning no jets are detected in the event, is the most important branch in the Higgs analysis since it contains a very little amount of the top background. Radiating quarks and gluons in a Higgs event can contribute to ggF production events in the $N_{jet} = 1$ bin but appear mainly in the $N_{jet} = 0$ bin. The bins with $N_{jet} \geq 2$ will contain Higgs events produced by VBF-production since its final state of particles have two high energetic jets.

The cut that requires $N_{jet} = 0$ events, called jet-veto, reduces all background containing jets in their final states, such as the top background. As can be seen in figure 5.9 the DY background is dominating in SF events for $N_{jet} \leq 1$ whereas the top background is dominating in all lepton flavour events for $N_{jet} \geq 2$. The WW background from SM production is mostly seen in DF events in the bins with $N_{jet} \leq 1$ at this stage of the analysis.

In order to reduce Drell-Yan background a variable called f_{recoil} is introduced in the same flavour channel, which measures the hadronic recoil produced in the opposite direction of the dilepton system. Since neutrinos are not produced in a Drell-Yan process, this variable will be large for the background but not for a real Higgs event. An alternative measurement of the missing transverse energy, calculated from tracks in the inner detector, $E_T^{miss}(trk)$, is also introduced. Another cut to further reduce the Drell-Yan background while retaining majority of the signal is the requirement of $P_T^{ll} > 30$ GeV in the $N_{jet} = 0$ branch.

For the branches containing jets further cuts are needed such as b-jet veto and $Z_{\tau\tau}$ veto. The b-jet veto cut is applied to suppress the top background and rejects all events containing any b-tagged jets. $Z_{\tau\tau}$ veto is applied to reduce the events from the background of $Z \to \tau\tau$. This cut is similar to the Z-veto cut in pre-selections and rejects event where $|m_{\tau\tau} - m_Z| < 25$ GeV. The jet multiplicity cuts are summarised in the first part of table 5.2.

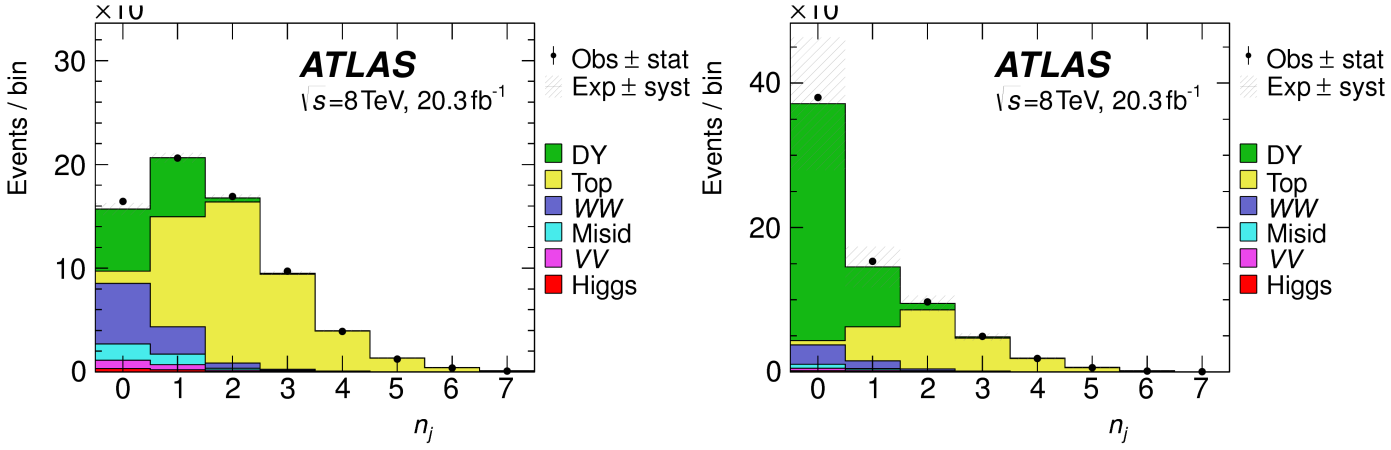

(a) Jet multiplicity with DF Leptons

(b) Jet multiplicity with SF Leptons

Figure 5.9: Event selection after the pre selection cuts with jet multiplicity divided into different flavour leptons (a) and same flavour leptons (b). Drell-Yan is dominating for SF events in the $N_{jet} \leq 1$ bins and the top background is dominating in the $N_{jet} \geq 2$ bins. Figure credit [39].

5.4.3 Topological Cuts

The topological cuts is the last part of the event selection and is done to further suppress the different backgrounds, where the main background for the topological cuts is the SM WW background. Since the signal from a Higgs event will have leptons propagating in the same direction, the topological cuts will have constraints on the opening angle between the two leptons in order to reduce the SM WW background. The topological cuts are divided in the three jet multiplicity branches and are summarised in table 5.2.

The main variable for the topological cuts are:

- $\Delta\phi_{ll}$, the opening angle between the two charged leptons in the transverse plane.
- $\Delta\phi_{ll,E_T^{miss}}$, the opening angle between the dilepton system and E_T^{miss}.
- m_{ll}, the invariant mass for the two leptons.

Table 5.2: Summary of the jet multiplicity and topological cuts divided into the number of jets found in the event. The first five variables belongs to the jet multiplicity cuts and the last three belongs to the topological cuts.

Variable	$N_{jet} = 0$	$N_{jet} = 1$	$N_{jet} \geq 2$
P_T^{ll}	≥ 30 GeV	-	-
f_{recoil}	< 0.1 (SF)	< 0.1 (SF)	< 0.1 (SF)
E_T^{miss}(trk)	> 40 GeV (SF)	> 35 GeV (SF)	> 35 GeV (SF)
b-jet veto	-	$N_{b-jet} = 0$	$N_{b-jet} = 0$
$Z_{\tau\tau}$ veto	-	$\lvert m_{\tau\tau} - m_Z \rvert < 25$ GeV	$\lvert m_{\tau\tau} - m_Z \rvert < 25$ GeV
$\Delta\phi_{ll}$	$< \frac{\pi}{2}$	$< \frac{\pi}{2}$	$< \frac{\pi}{2}$
$\Delta\phi_{ll,E_T^{miss}}$	$> \frac{\pi}{2}$	-	-
m_{ll}	< 55 Gev	< 55 Gev	< 55 Gev

5.5 Background Estimation

A common method to normalise the background from Monte Carlo predictions is to compare it with so called control regions, CR. Control regions are regions where the data almost entirely consists of the background to be normalised. The normalisation factor is then extrapolated to the signal region, SR, where the correct number of events for the background is needed [40]. It is defined by:

$$N_{SR} = \left(\frac{N_{SR}^{MC}}{N_{CR}^{MC}}\right) \cdot \left(N_{CR}^{data} - N_{CR}^{other}\right) \tag{5.3}$$

where N_{SR} is the extrapolated number of events in the signal region, N_{CR}^{MC} and N_{SR}^{MC} are events in the control region respectively signal region predicted by Monte-Carlo simulations, N_{CR}^{data} is number of events of the background to be normalised in the control region, and N_{CR}^{other} is other contributions to the data in the control region.

In order to reduce chances of being biased, the analysis is done blinded. Once the analysis is completed the data is unblinded meaning that the results will be known first once the analysis is done.

5.5.1 WW Background and Control Region

One of the leading background from Standard Model processes producing two isolated leptons with high P_T is the SM WW background. In order to estimate the background MC-predictions are normalised as in Eq. (5.3) to the data in control regions as described above. The SM WW CR is defined by using the same cuts as in the event selection for the Higgs analysis except for the variables displayed in table 5.4.

Table 5.3: Summary of cuts designed specifically for the SM WW control region divided in number of jets.

Cuts:	$N_{jet} = 0$	$N_{jet} = 1$
m_{ll}	$50 < m_{ll} < 100$ GeV	$80 < m_{ll}$ GeV
$P_T^{sublead}$	> 15 GeV	> 15 GeV
$\Delta\phi_{ll}$	< 2.6	-

The signal region and control region is separated over the range of the dileptonic mass, m_{ll}. Ideally, CR is set as the region where the relevant background is dominating. However, in same flavour events the Drell-Yan background is more dominating, which means that only different flavour events are used in the normalisation of the SM WW background. In the same way are estimations for data with $N_{jet} \geq 2$ only made with MC-predictions since there is no dominating region for the SM WW background for $N_{jet} \geq 2$.

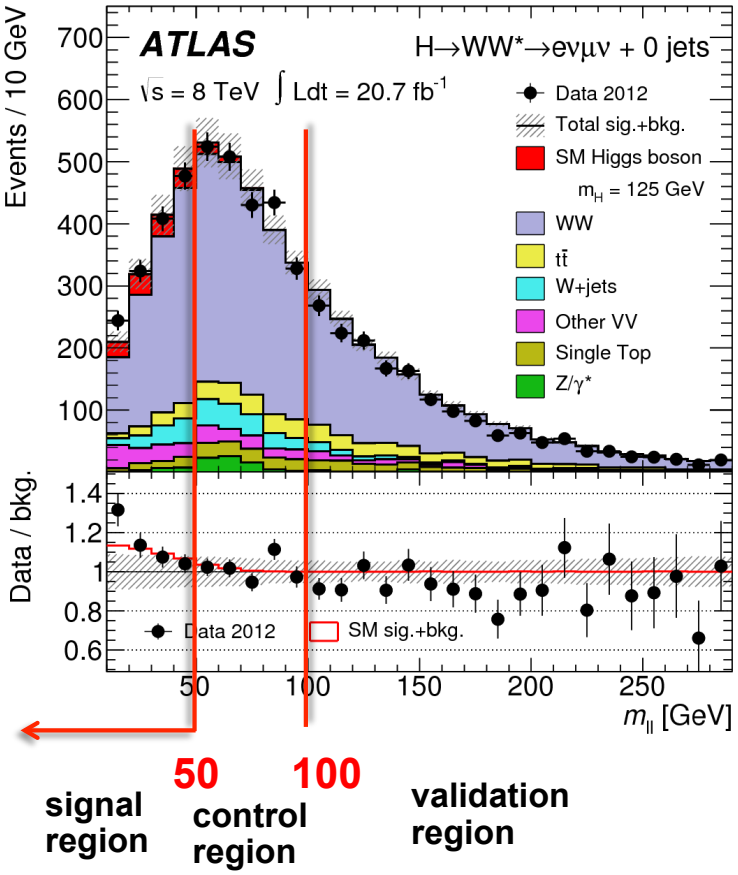

Figure 5.10: Dileptonic mass distribution for 8 TeV data illustrating the signal, control, and validation regions from ATLAS. Figure credit [41].

As can be seen in figure 5.10 the control region for $N_{jet} = 0$ is right next to the signal region and even containing a small amount of signal. This is to reduce the systematic error that occurs when extrapolating from CR to SR since there is (likely) a systematic shift for WW in m_{ll} . The control region was at first defined at a higher m_{ll} region since the WW background is dominating there. This turned out to underestimate the background leading the normalised background in the signal region to be too low. The normalisation factor, calculated comparing the predicted background and data in the control region, is calculated as $N_f = 1.22$ for the WW background in the $N_{jet} = 0$ branch and scales up the rest of the background to fit the data over all regions. There is still a small excess of data compared to the predicted background after normalisation at low m_{ll} for WW background and further kinematic distributions as the m_{ll} distribution will be discussed in chapter 6.

5.6 Results

The results of the event selection cuts for $N_{jet} = 0$ is displayed by the cutflow tables in Table 5.4 for DF events and 5.5 for SF events. A cutflow table shows the number of events from expected and observed signal and background events after each cut.

The columns containing N_{obs}, N_{bkg} and N_{sig} are the summarised yields for expected and observed events where N_{obs} is observed yields, N_{bkg} is the expected background yields and N_{sig} is the expected signal yields. The five last columns, N_{WW}, N_{top}, N_{misid}, N_{VV} and N_{DY}, are the dominating backgrounds, described above, normalised by control regions.

It can be seen in both cutflow tables that N_{obs} is higher than N_{bkg} after the last cut. The difference corresponds well with the expected signal from a Higgs event N_{sig} after the same cut [5].

The final data after normalisation of backgrounds of the transverse mass distribution of combined data for $N_{jet} \leq 1$ and with both SF and DF events is displayed in figure 6.2

The data is statistically treated by a likelihood function which is based on two hypotheses. The first hypothesis is that all data observed corresponds only to the background from Standard Model processes. The second hypothesis states that the data also contains signal from Higgs production events. The excess of the data, that is displayed as red in figure 5.11, is the signal of the Higgs boson and corresponds to a significance of 6.1 standard deviations that the second hypothesis is true. Meaning there is a $1/(5 \cdot 10^8)$ chance that the same data would be collected if the first hypothesis was true.

Table 5.4: Cutflow table for the $N_{jet} = 0$ branch for event selection at $\sqrt{s} = 8$ TeV with $e\mu$-leptons from ATLAS.

Selection:	N_{obs}	N_{bkg}	N_{sig}	N_{WW}	N_{top}	N_{misid}	N_{VV}	N_{DY}
$N_{jet} = 0$	16423	16330	290	7110	1227	1567	739	5685
$\Delta\phi_{ll,E_T^{miss}} > \frac{\pi}{2}$	16339	16270	290	7110	1217	1560	736	5644
$P_T^{ll} \geq 30$ GeV	9339	9280	256	5690	1093	1082	571	843
$m_{ll} < 55$ Gev	3411	3060	224	1670	220	439	353	377
$\Delta\phi_{ll} < \frac{\pi}{2}$	2642	2350	203	1500	207	287	324	31

Table 5.5: Cutflow table for the $N_{jet} = 0$ branch for event selection at $\sqrt{s} = 8$ TeV with $ee/\mu\mu$-leptons from ATLAS.

Selection:	N_{obs}	N_{bkg}	N_{sig}	N_{WW}	N_{top}	N_{misid}	N_{VV}	N_{DY}
$N_{jet} = 0$	38040	36520	163	3260	629	533	358	31745
$\Delta\phi_{ll,E_T^{miss}} > \frac{\pi}{2}$	35445	33890	163	3250	627	519	355	29142
$P_T^{ll} \geq 30$ GeV	11660	11040	154	3010	595	399	309	6721
$m_{ll} < 55$ Gev	6786	6710	142	1260	173	253	179	4849
E_T^{miss}(trk) > 40 GeV	2197	2160	117	1097	158	133	106	660
$\Delta\phi_{ll} < \frac{\pi}{2}$	2127	2100	113	1068	153	122	104	644
$f_{recoil} < 0.1$	1108	1096	72	786	72	79	69	91

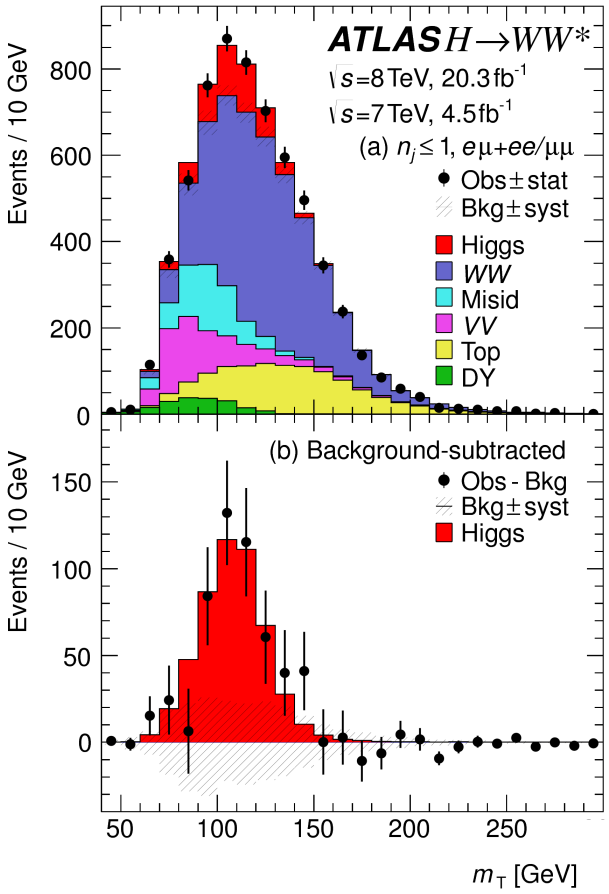

Figure 5.11: Final result of the transverse mass distribution for combined 7 and 8 TeV data for $N_{jet} \leq 1$ and both SF and DF events from ATLAS with a 6.1σ signal of a Higgs boson [5].

Chapter 6

Investigation of the WW excess

6.1 The WW excess

The WW background described in 5.2.1 and 5.4.1 is scaled by a normalisation factor, N_f, to account for the difference between detected data and MC predictions. Normalisation factors are calculated individually for each background from its control region and then extrapolated to the signal region with eq (5.3). For the WW background this factor has turned out to be quite large, up to N_f=1.22 (in the ATLAS SM analysis).

Table 6.1 display the normalisation factors for the WW background in the Higgs analysis for 7 TeV and 8 TeV from CMS and ATLAS. Both have calculated high normalisation factors and there is a small increase of the factor from 7 TeV to 8 TeV data [3][4].

Table 6.1: Normalisation factor of the WW background in the Higgs analysis from CMS and ATLAS for $\sqrt{s} = 7$ TeV and $\sqrt{s} = 8$ TeV.

$\sqrt{s}$:	7 TeV	8 TeV
CMS	N_f=1.10	N_f=1.12
ATLAS	N_f=1.13	N_f=1.16

In the Standard Model analysis at CMS and ATLAS there is also an inconsistency with the detected and predicted cross section for the WW background. Both detected higher cross section in data than was predicted by MC simulations, see table 6.2 [36]. In fact, the cross section measurements from CMS and ATLAS are more consistent with the measurements of each other than with the predictions from SM. However, this has not been the topic of research at the time and the WW background has been multiplied with 1.2 in order for it to be sufficiently accurate to be justified and used.

This was the status in the beginning of this master thesis project. There is a clear and well known discrepancy which nobody knew the reason for.

Table 6.2: Cross section from observed measurements and expected predictions with MC in ATLAS and CMS for 7 TeV and 8 TeV measured in picobarn.

		$\sqrt{s} = 7$ TeV	$\sqrt{s} = 8$ TeV
ATLAS:	Expected:	$\sigma = 47.04^{+2.02+0.90}_{-1.51-0.66}$ pb	$\sigma = 57.25^{+2.35+1.09}_{-1.60-0.8}$ pb
	Observed:	$\sigma = 51.9^{2.0+3.9+2.0}_{-2.0-3.9-2.0}$ pb	$\sigma = 71.4^{+1.2+5.0+2.2}_{-1.2-4.4-2.1}$ pb
CMS:	Expected:	$\sigma = 47.04^{+2.02+0.90}_{-1.51-0.66}$ pb	$\sigma = 57.25^{+2.35+1.09}_{-1.60-0.8}$ pb
	Observed:	$\sigma = 52.4^{+2.0+4.5+1.2}_{-2.0-4.5-1.2}$ pb	$\sigma = 69.9^{+2.8+5.6+3.1}_{-2.8-5.6-3.1}$ pb

6.2 Other physics processes

A simple answer to this discrepancy would be that the theoretical calculations of cross section at LHC are wrong. However, the theoretical calculations for the WW cross section and the ZZ cross section are in general executed in the same way. Which means that if there was a simple explanation to this excess there would be other discrepancies visible for other cross section measurements as well. This is not the case which can be seen in figure 6.1 displaying ATLAS results of the cross section ratio between observed measurements and theoretical predictions. For the 8 TeV data, displayed by red rods in the figure, the ZZ cross section has a ratio between measured data and theory prediction aligned with one, whereas the WW cross section ration is not even with its range of uncertainty close to the ratio one.

Excesses are not seen for otherwise theoretically similar processes either. Figure 6.2 is summarising all measurements for $N_{jet} \leq 1$ and all leptonic flavour events for the $H \rightarrow WW$ analysis. No tendencies are visible of any shape variation discrepancies here either. This indicates, as written above, that there is no simple single answer to why there is an excess in the WW background compared to predictions.

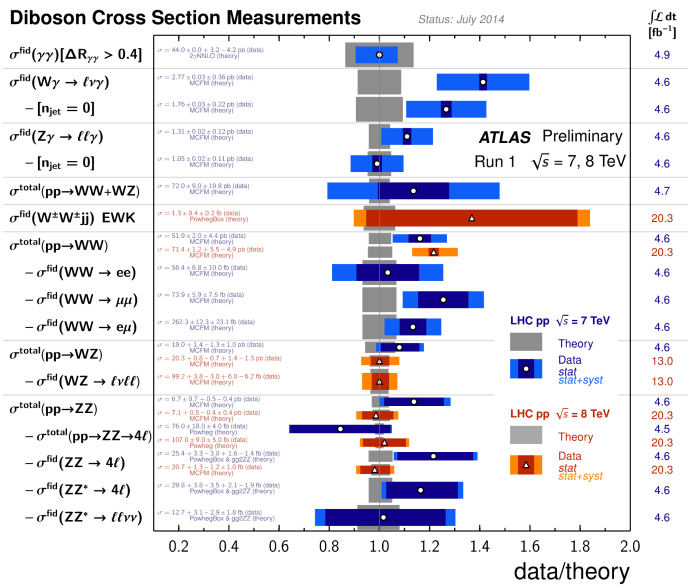

Figure 6.1: Ratio of measured and predicted cross sections for different processes from ATLAS where blue rods are 7 TeV data and red rods are 8 TeV data [42].

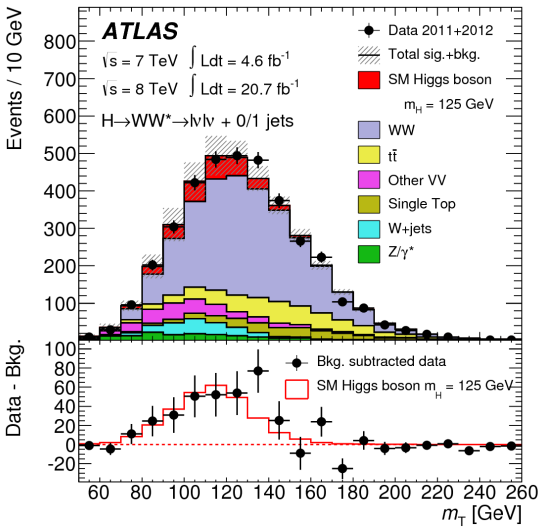

Figure 6.2: Summarised measurements of data with all leptonic flavours and $N_{jet} \leq 1$ in the $H \rightarrow WW$ analysis at ATLAS with $\sqrt{s}$ of 7 TeV and 8 TeV [5].

6.3 Developments during the year of 2014

It turned out that this problem was more popular than first expected. During the summer of 2014 when this project started, the WW excess became a hot topic in the literature trying to explain it.

A paper called "Charginos hiding in plain sight" by Curtin, Jaiswal, and Meade [43], put forward the idea that the excess could originate from Super Symmetry. SUSY would provide new physics that only affect the EW cross section measurements. This is because light EW-inos, also called Charginos, may have a bound at $\mathcal{O}(100$ GeV) whereas coloured particles of $\mathcal{O}$(TeV). The results of the effect of Charginos is shown in figure 6.3. Even though SUSY is a popular explanation to the WW excess, it should give rise to more signal as discrepancies other than only this.

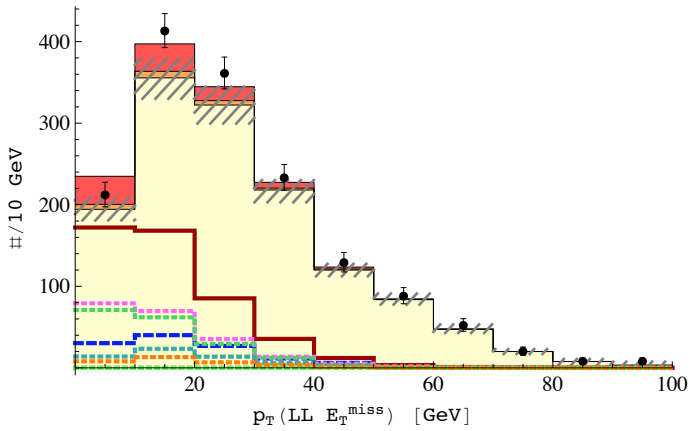

Figure 6.3: P_T distribution of the SM predictions, in yellow, from atlas 7 TeV data with additional contribution from $H \rightarrow WW$, in orange, and chargino production, in red [43].

New physics is a possible explanation for this excess, but most experimentalists favour explanations where the discrepancy originates in some deficiency of the theoretical calculations of the cross section. In figure 6.4, where the MC predictions are compared with measured data at 8 TeV as a function of jet multiplicity, it is clear that the excess discrepancy is mainly in the $N_{jet} = 0$ bin.

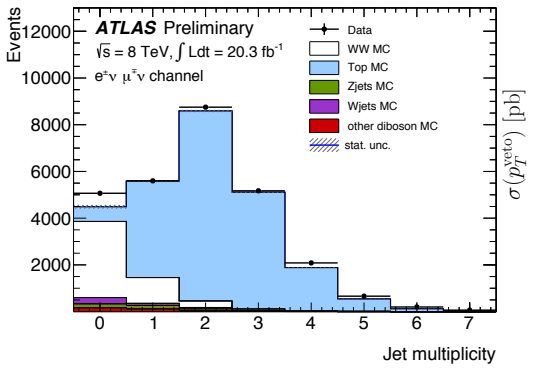

Figure 6.4: Comparison of measured data and MC predictions as a function of jet multiplicity at 8 TeV for events with different flavoured leptons [7].

Discussions about how much effect the extrapolation of the fiducial cross section to the total inclusive cross section had on the observed excess became a popular area. This extrapolation relies on MC simulations with a fixed mass scale for the pair of W bosons, m_{WW}. It is well known though that this kind of fixed order calculations in general underestimates the theoretical uncertainty. However, the question is if this effect is negligible.

The extrapolation to the total inclusive cross section rejects jets with a P_T greater than a set value P_T^{veto} ("jet-veto"). For ATLAS P_T^{veto} is set to 25 GeV and for CMS $P_T^{veto} = 30$ GeV. This is a necessary evil in order to reduce the top background.

A suggested model, called "jet-veto resummation", was to introduce a new mass scale, P_T^{veto}, in addition to the m_{WW} scale. In figure 6.5 the effect of the new added P_T^{veto} scale is displayed where the jet-veto resummation cross sections are compared with the measured crossections at CMS and ATLAS. It shows that the new predicted cross sections with jet-veto resummation give rise to explaining about 3 % of the cross section excess [44].

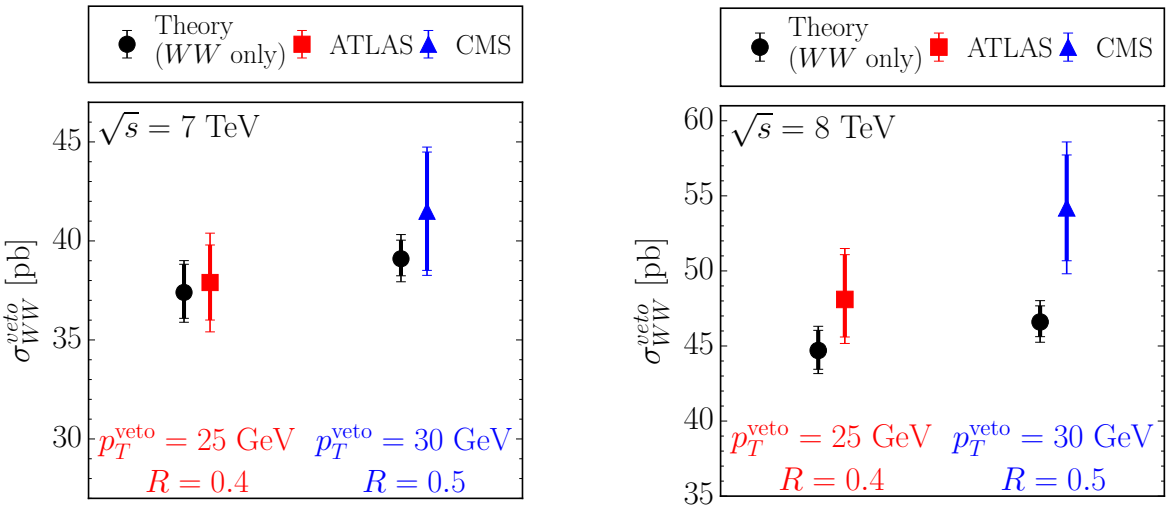

(a) $\sqrt{s} = 7$ *TeV* *(b)* $\sqrt{s} = 8$ *TeV*

Figure 6.5: Theory predictions computed with jet veto resummation compared with ATLAS and CMS measured cross sections at (a) $\sqrt{s} = 7$ *TeV and (b)* $\sqrt{s} = 8$ *TeV [44].*

Another model, called P_T-resummation, discussed adding a new mass scale depending on the transverse momentum of the W bosons, P_T^{WW}, instead of P_T^{veto}. P_T-resummation uses expansion when extrapolating with $\log \frac{m_{WW}}{P_T^{WW}}$ instead of $\log \frac{m_{WW}}{P_T^{veto}}$ as jet-veto resummation does. This is easier to calculate with since P_T^{WW} can be measured from the detectors, but is further away from the source of truth than jet-veto resummation [45].

In figure 6.6 the results of the P_T-resummation effect can be seen. For large P_T, the fixed order calculations are valid. But for lower values of P_T, P_T resummations are more compatible with the observed data and can explain up to 3-7% of the cross section excess.

Overall, these two resummation models with adding a new mass scale can explain 3-7% of the excess discrepancy, but does not explain all of it.

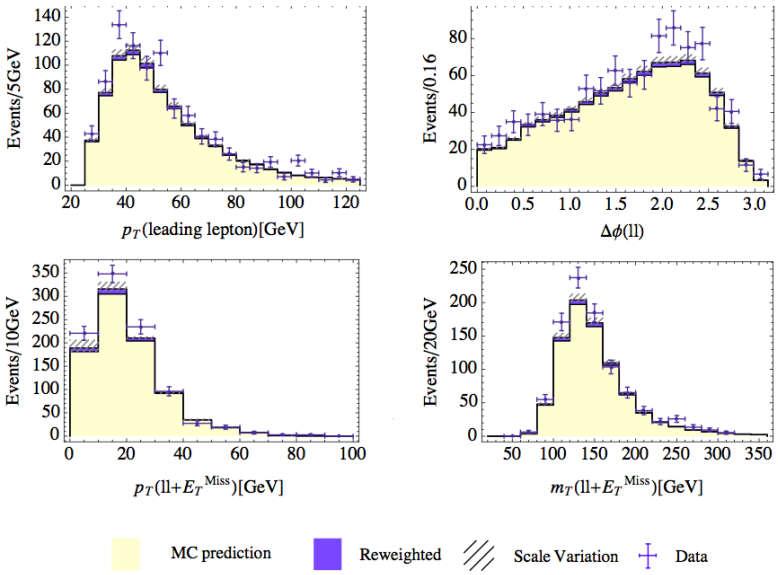

Figure 6.6: Measured data from ATLAS compared with MC predictions (in yellow) and the effect of reweighing the mass scale with P_T resummation (in purple) added [45].

Another approach of tackling the excess problem was to look at the computed orders of calculations for WW production at LHC. So far only leading order, LO, and next-to-leading order, NLO, calculations had been computed, which does not include productions beyond NLO.

A new level of accuracy with NNLO (next-to-next-to-leading order) calculations were computed and the results are shown in figure 6.7. It turns out that NNLO calculations can describe the excess for the 7 TeV data and most of the excess for the 8 TeV data. This is so far the best explanation to the excess and it will be interesting to compare the 13 TeV data from run 2 that is being collected at LHC at the moment [46].

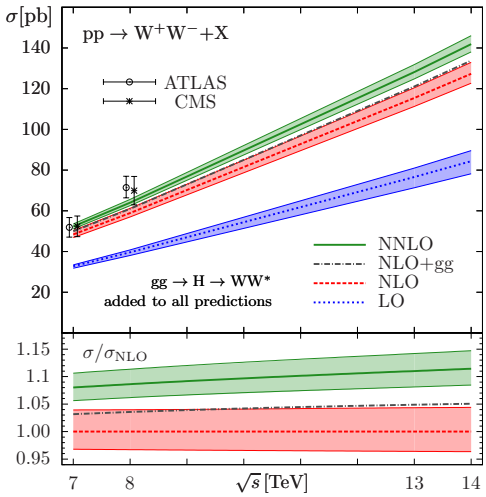

Figure 6.7: The WW cross section as a function of $\sqrt{s}$ at LO, NLO and NNLO compared to the measured cross sections from CMS and ATLAS [46].

6.4 Systematic classification of the WW excess

The goal of this study was to see if there is a systematic way to classify the WW excess described above.

This consistency of getting a high value of N_f for the WW background has been known throughout the history of the Higgs analysis. In the beginning of the control region for the WW background was defined at the range of $m_{ll} > 80$ GeV in the $N_{jet} = 0$ branch as well as in the $N_{jet} = 1$ branch. This was logical since this region does not contain any signal and the WW background is the dominating background for $m_{ll} > 80$ GeV.

Even though it improved the statistical uncertainty, the systematic uncertainty increased when extrapolating to the signal region. Looking at figure 5.10 it is clear that having the control region at higher m_{ll} underestimated the background, and the control region got because of this moved closer to the signal region. It rose the question of if other kinematic distributions in the Higgs analysis had similar shape variation discrepancies.

Kinematic distributions with a dominating WW background in the Higgs analysis from ATLAS got singled out and analysed. These distributions had already been normalised and scaled to fit the data, a general excess is therefore not what was looked for. The question in hand was instead to investigate possible shape variations in the distributions.

Figure 6.8 is an example of the shape discrepancy of the dileptonic mass distribution, m_{ll}. It has the same tendency as in figure 5.10 with excess at low m_{ll} range and deficit at high m_{ll} range, even though the distribution has already been normalised. The data is perfectly aligned with the predicted values for $50 < m_{ll} < 100$ GeV, which is another sign of the discrepancy having its origin in the WW background.

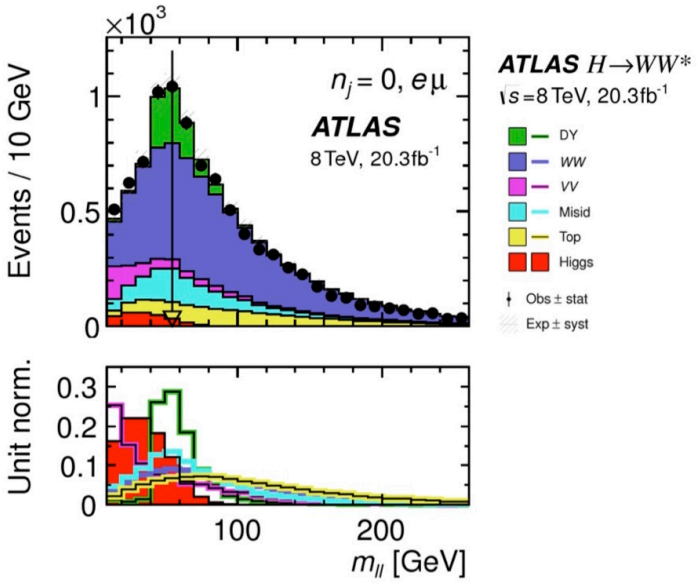

Figure 6.8: Distribution of m_{ll} for $N_{jet} = 0$ and DF leptons in the $H \to WW$ analysis for $\sqrt{s} = 8$ TeV from ATLAS. The data can be seen to overshoot the background at low values of m_{ll}, and undershoot the background at high values, indicating a mismodelling of the WW background which cannot be explained by a simple scaling of the background [5].

Several other kinematic distributions with dominating WW background were looked at, which mainly means distributions in the $N_{jet} = 0$ bin. This is because the top and DY backgrounds are too overwhelming for higher jet multiplicities to draw any valid conclusions.

There were however no tendencies of any excess or shape variations for the other kinematic distributions similar to the m_{ll} discrepancy. For instance in figure 6.9, displaying the P_T distribution of the dileptonic system, it is clear that observed data and MC predictions for P_T values agree very well with each other. No indications of any irregularities in the shape of the data compared to the predictions could be seen.

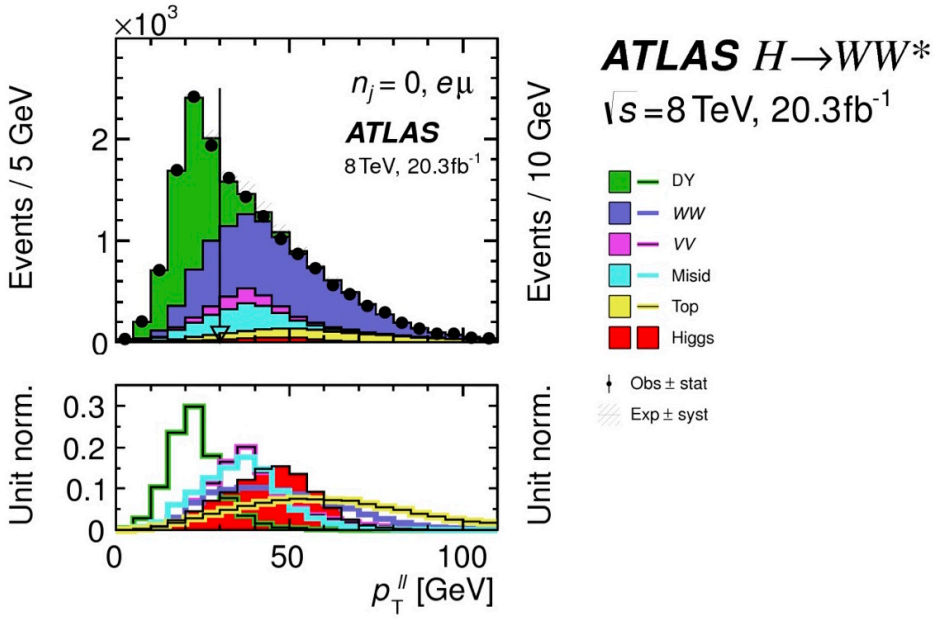

Figure 6.9: Distribution of P_T for $N_{jet} = 0$ and DF leptons in the $H \to WW$ analysis for $\sqrt{s} = 8$ TeV from ATLAS. Good agreement can be observed between the data and predicted WW shape for all values [5].

The transverse mass distributions did not show any shape variation tendencies either and as figures 6.10 and 6.11 shows there were no significant differences between 7 TeV and 8 TeV data. The observed data agrees a bit more with the expected predictions for the 8 TeV data, in figure 6.11, but this is probably just due to the fact of it having higher luminosity. There does not seem to be any difference of tendencies to shape discrepancies wether the final leptons are of different or same flavour. Examples of this can also be seen in figures 6.10 and 6.11.

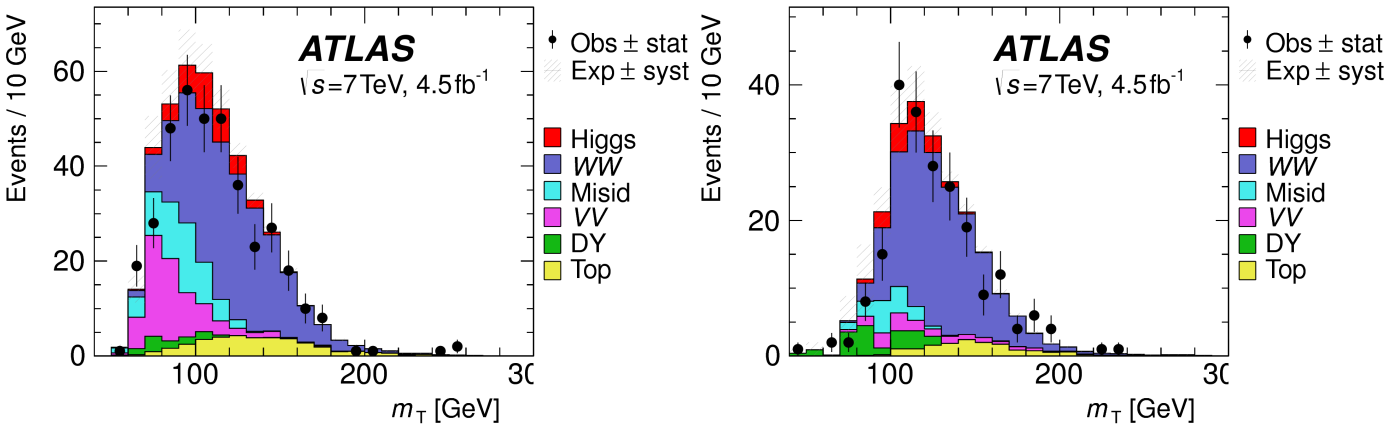

(a) m_T distribution with DF Leptons *(b) m_T distribution with SF Leptons*

Figure 6.10: Distribution of the transverse mass for N_{jet}=0 in the Higgs analysis at ATLAS of 7 TeV data with (a) eμ/μe and (b) ee/μμ. Reasonable agreement, considering the statistical uncertainties, can be observed between the data and the predicted WW shape for all values [5].

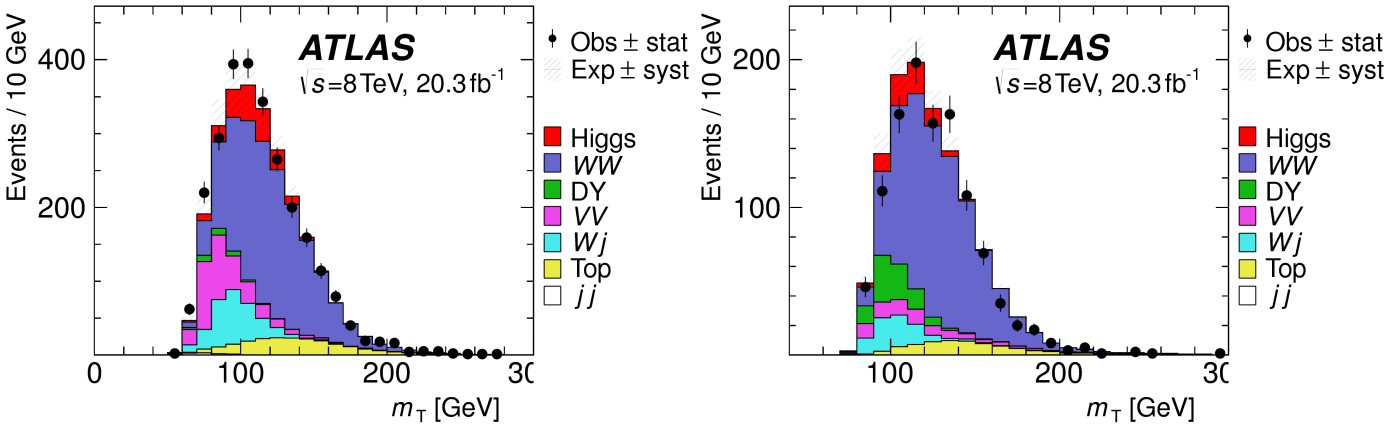

(a) m_T distribution with DF Leptons *(b) m_T distribution with SF Leptons*

Figure 6.11: Distribution of the transverse mass for N_{jet}=0 in the Higgs analysis at ATLAS of 8 TeV data with (a) eμ/μe and (b) ee/μμ. Reasonable agreement, considering the statistical uncertainties, can be observed between the data and the predicted WW shape for all values [5].

6.5 Conclusions of the findings

The excess seems to be mostly explained by the missing components in the early theoretical calculations. Adjusting the approximation of using a fixed mass scale by resummation can only explain about 3-7 % of the excess though. Computation of cross section with higher order up to NNLO seemed to explain the excess observed in the 7 TeV data and a majority of the excess in 8 TeV data.

It will be interesting to compare the results with the 13 TeV data that is being collected at LHC at the moment. It would also be interesting to see if the same effects can be seen in other analyses requiring a veto on additional jets.

For the investigation of shape variations of the kinematic distributions, there were only noticeable discrepancy in the m_{ll} distribution. Whereas the other kinematic distributions showed no irregularities comparing to data after being normalised and no difference for the different leptonic flavours. The m_{ll} distribution had still, even after normalisation, excess in data for low range of m_{ll} but a deficit in data for high range of m_{ll}.

Even though most of the excess discrepancy can be explained by new NNLO calculations, it is not obvious that the discrepancy of the m_{ll} shape distribution can be explained by the updated theoretical calculations.

Chapter 7

Conclusions

In the year of 2014, there was a problem in the cross section measurement of the SM WW process and the normalisation of the same process in the $H \to WW$ analyses. In both cases, the WW cross sections, measured by the CMS and ATLAS experiments at LHC, found to be higher than the SM predictions by about 20 %.

The goal of this thesis project was to investigate the problem of WW excess and try to classify the discrepancy by looking for tendencies of shape variations in different kinematic distributions from the $H \to WW$ analysis at ATLAS. This turned out to be a hot topic during the summer of 2014. Several attempts were made in the literature to explain the excess by discussing missing components in the theoretical calculations of the cross section.

The addition of a new mass scale when calculating the fiducial cross section could, at the most, explain 3-7 % of the excess. Higher order of calculations had more impact on the predicted cross section than was expected. It could explain a majority of the excess for the $\sqrt{s} = 8$ TeV data but not all of it.

There were no tendencies of shape variations in the kinematic distributions from the $H \to WW$ after normalisation, expect for in the m_{ll} distribution. The data in the control region of the m_{ll} distribution agrees very well with the SM prediction after normalisation but has a clear excess at m_{ll} values below the control region and deficit at higher m_{ll} values.

To conclude, theoretical computation of NNLO calculations can explain most of the excess. However, the problem of the shape discrepancy of the m_{ll} distribution still stands. Further investigations of the analysis with 13 TeV data would be interesting. Perhaps new shape differences can be observed with larger statistics expected at $\sqrt{s} = 13$ TeV.

Acknowledgements

I would like to express my very great appreciation to my supervisor Jonas Strandberg for giving me the opportunity to do this thesis. From guiding and teaching me about the research to supporting and pushing me throughout the process. I wish to thank Bengt Lund-Jensen for helping me stay positive along the way and making this thesis possible. I am very grateful to Edvin Sidebo for answering my questions and to Björn Ahlgren for the support. I am also grateful to Nabila Shaikh and Cecilia Nyström for their help in answering my questions and to Giulia Ripellino for being such an inspiration. Finally I would like to thank my family and close friends for all their love and support.

List of Figures

List of Tables

Bibliography

[1] CMS Collaboration. *Observation of a new boson at a mass of 125 GeV with the CMS experiment at the LHC.* Physics Letters B, Volume 716, September 2012.

[2] ATLAS Collaboration. *Observation of a new particle in the search for the Standard Model Higgs boson with the ATLAS detector at the LHC.* Physics Letters B, Volume 716, September 2012.

[3] The ATLAS Collaboration. *Measurements of the properties of the Higgs-like boson in the $WW^{(*)} \to \ell\nu\ell\nu$ decay channel with the ATLAS detector using 25 fb^{-1} of proton-proton collision data.* ATLAS-CONF-2013-030, CERN, Geneva, Mar 2013.

[4] The CMS Collaboration. *Measurement of the WW production cross section in pp collisions at $\sqrt{s} = 8$ TeV.* CMS PAS SMP-12-013.

[5] The ATLAS Collaboration. *Observation and measurement of Higgs decays to WW^* with the ATLAS detector.* ATLAS-CONF-2014-060, October 2014.

[6] The CMS Collaboration. *Measurement of Higgs boson production and properties in the WW decay channel with leptonic final states* CMS-HIG-13-023, December 2013

[7] The ATLAS Collaboration. *Measurements of the WW production cross section in proton-proton collisions at $\sqrt{s} = 8$ TeV with the ATLAS detector.* ATLAS-CONF-2014-033, CERN, Geneva, July 2014.

[8] The CMS Collaboration. *Measurement of WW and ZZ production cross sections in pp collisions at sqrt(s)=8 TeV* CMS-SMP-12-024, January 2013

[9] Martin, B.R. and Shaw, G. *Particle Physics.* Wiley, 2012.

[10] Glashow, S.L. *Partial Symmetries of Weak Interactions.* Nuclear Physics B, Volume 22, February 1961.

[11] Weinberg, S. *A Model of Leptons.* Physical Review Letters, Volume 19, November 1967.

[12] Englert, F. and Brout, R. *Broken symmetry and the mass of gauge vector mesons.* Physical Review Letter, Volume 13, August 1964.

[13] Higgs, P. *Broken symmetries, massless particles and gauge fields.* Physics Letters, Volume 12, September 1964.

[14] Guralnik, G.S., Hagen, C.R., and Kibble, T.W.B. *Global conservation laws and massless particles.* Physical Review Letter, Volume 13, November 1964.

[15] 't Hooft, G. and Veltman, M. *Regularization and renormalization of gauge fields.* Nuclear Physics B, Volume 44, July 1972.

[16] Fukuda, Y. et al. *Evidence for Oscillation of Atmospheric Neutrinos.* Physical Review Letters, Volume 81, August 1998.

[17] Griffiths, D. *Introduction to Elementary Particles.* Wiley-VCH, 2008.

[18] Henley, E.M. and Garcia, A. *Subatomic Physics.* World Scientific Pbl, 2012.

[19] Schwinger, J. *A Theory of the Fundamental Interactions.* Annals of Physics, Volume 2, November 1957.

[20] Cabibbo, N. *Unitary Symmetry and Leptonic Decays.* Physical Review Letters, Volume 10, June 1963.

[21] Baggot, J. *Higgs: The invention and discovery of the 'God Particle'.* UP Oxford, 2012.

[22] Higgs, P. *Broken symmetries and the masses of gauge bosons.* Physical Review Letter, Volume 13, October 1964.

[23] Álvarez-Gaumé, L. and Ellis, J. *Eyes on a prize particle* Nature Physics, Volume 7, December 2010.

[24] Townsend, J.S. *A Modern Approach to Quantum Mechanics.* s. 218-219, University Science Books, 2000.

[25] CERN *WLCG: Worldwide LHC Computing Grid.* `wlcg.web.cern.ch`

[26] CERN *About CERN.* `home.web.cern.ch`

[27] Evans, L. and Bryant, P *LHC machine.* Journal of Instrumentation, Volume 3, August 2008.

[28] TheATLAS Collaboration. *Improved luminosity determination in pp collisions at sqrt(s) = 7 TeV using the ATLAS detector at the LHC.* Eur.Phys.J. C73 (2013) 2518.

[29] Binoth, T. et al. *LHC Physics.* CRC Press Taylor & Francis Group, 2012.

[30] The ATLAS Collaboration. *The ATLAS experiment at the CERN Large Hadron Collider.* Journal of Instrumentation, Volume 3, August 2008.

[31] The ATLAS Collaboration. *Detector Description.* `atlas.ch/detector.html`

[32] Mets501 *Pseudorapidity* Wikipedia.org, 24 July 2012.

[33] Baglio, J. and Djouad, A. *Higgs production at the LHC.* Journal of High Energy Physics, Volume 2011, 2011.

[34] The LHC Higgs Cross Section Working Group. *Handbook of LHC Higgs Cross Sections: 3. Higgs Properties.* arXiv:1307.1347v2 [hep-ph].

[35] Denner, A. et al. *Standard Model Higgs Boson Branching Ratios with Uncertainties.* arXiv:1107.5909v2, July 2011.

[36] The LHC Cross section Working Group, et al. *Handbook of LHC Higgs Cross Sections; 3, Higgs Properties.* CERN-2013-004, July 2013.

[37] Beringer, J. et al. (Particle Data Group). *Status of Higgs Boson Physics.* Physical Review Letter, Volume 86, 2012.

[38] The ATLAS Collaboration. *Study of the spin properties of the Higgs-like particle in the $H \to WW^{(*)} \to e\nu\mu\nu$ channel with 21 fb^{-1} of $\sqrt{s} = 8$ TeV data collected with the ATLAS detector.* ATLAS-CONF-2013-031, CERN, Geneva, March 2013.

[39] The ATLAS Collaboration. *Observation and measurement of Higgs boson decays to WW^* with the ATLAS detector.* Phys. Rev. D 92, 012006.

[40] The HWW Working Group. *Background Estimates in the $H \to WW^* \to l\nu l\nu$ Analysis with 20 fb^{-1} of Data Collected with the ATLAS Detector at $\sqrt{s} = 8$ TeV.* ATLAS-COM-PHYS-2013-1630, April 2014.

[41] The ATLAS Collaboration. *Measurements of Higgs boson production and couplings in diboson final states with the ATLAS detector at the LHC.* Phys. Lett. B 726.

[42] The ATLAS Collaboration. *Measurements of Wgamma and Zgamma production in pp collisions at $\sqrt{s} = 7$ TeV with the ATLAS detector at the LHC.* arXiv:1302.1283, 2013

[43] Curtin, D., Jaiswal, P., and Meade, P. *Charginos Hiding in Plain Sight.* arXiv:1206.6888, August 2012.

[44] Jaiswal, P. and Okui, T. *An Explanation of the WW Excess at the LHC by Jet-Veto Resummation.* arXiv:1407.4537v4, January 2015.

[45] Meade, P., Ramani, H., and Zeng, M. *Transverse momentum resummation effects in W^+W^- measurements.* arXiv:1407.4481v2, September 2014.

[46] German, T. et al. *W^+W^- production at hadron colliders in NNLO QCD.* arXiv:1408.5243v1, August 2014.